ENERGY LOSS OF LIGHT IONS CHANNELING IN SILICON

Thesis by

Jonathan David Melvin

In Partial Fulfillment of the Requirements

for the Degree of

Doctor of Philosophy

California Institute of Technology

Pasadena, California

1974

(Submitted May 31, 1974)

ACKNOWLEDGMENT

Thanks are due first of all to my advisor, Dr. Thomas Tombrello, for introducing me to the pleasures of experimental work, and for his constant guidance, interest, and willingness to discuss problems. Second, I wish to thank Dr. Frederick Eisen without whose experienced suggestions and excellent targets the experimental work would never have been possible.

Thanks also go to Dr. James Mayer for his constant willingness to teach me about the field of channeling, and for the many fruitful contacts he has made for me.

I also wish to give thanks to everyone in Kellogg Laboratory for creating an effective and friendly research community. I owe much of my experience in methods of experimental research and technology to many enjoyable discussions with members of the staff. In particular, I thank Lawrance Graham, to whom I owe a very helpful and practical knowledge of electronics.

Financial support was provided by the National Science Foundation and the California Institute of Technology. The National Science Foundation showed great flexibility in the administration of their support to me, for which I wish to express special gratitude.

Finally I wish to thank my California family whose constant support and help has allowed me to grow so much in my interest and commitment to scientific research.

ABSTRACT

Experimental measurements of rate of energy loss were made for protons of energy .5 to 1.6 MeV channeling through 1 μm thick silicon targets along the <110> , <111> , and <211> axial directions, and the {100} , {110} , {111} , and {211} planar directions. A .05% resolution automatically controlled magnetic spectrometer was used. The data are presented graphically along with an extensive summary of data in the literature. The data taken cover a wider range of channels than has previously been examined, and are in agreement with the data of F. Eisen, et al., Radd. Eff. 13, 93 (1972).

The theory in the literature for channeling energy loss due to interaction with local electrons, core electrons, and distant valence electrons of the crystal atoms is summarized. Straggling is analyzed, and a computer program which calculates energy loss and straggling using this theory and the Moliere approximation to the Thomas Fermi potential, V_{TF}, and the detailed silicon crystal structure is described. Values for the local electron density Z_{loc} in each of the channels listed above are extracted from the data by graphical matching of the experimental and computer results.

Zeroth and second order contributions to Z_{loc} as a function of distance from the center of the channel were computed from $\nabla^2 V_{TF} = 4\pi\rho$ for various channels in silicon. For data taken in this work and data of F. Eisen, et al., Rad. Eff. 13, 93 (1972), the calculated zeroth order contribution to Z_{loc} lies between the experimentally extracted Z_{loc} values obtained by using the peak and the leading edge of the

transmission spectra, suggesting that the observed straggling is due both to statistical fluctuations and to path variation.

TABLE OF CONTENTS

I. INTRODUCTION

The phenomenon of ions channeling in crystals provides a tool to study solid state structure. In this work the energy loss and straggling of 0^{o} transmitted channeling ions has been studied theoretically and experimentally in order to obtain a better understanding of the mechanism of energy loss and of the distribution of valence electrons in the crystal.

Channeling is the process of passage of a particle into or through a crystal in a planar or axial space of the crystal structure. Channeling ions penetrate deeper and pass through crystals with less energy loss than ions entering in a random direction because they have many fewer close encounters with nuclei and high density electron regions of the crystal atoms.

We will concern ourselves with light positive ions in the energy range 0.5 to 20 Mev. Such ions are guided primarily by interaction with crystal nuclei and lose energy primarily to crystal electrons. Because of the enormous number of atoms in the crystal, the theory of energy loss is necessarily approximate. For random transmission where crystal structure is not taken into account, there is the well established Bethe-Bloch theory. During the past decade much work has been done to develop a correspondingly good theory for channeling ions.

Lindhard (1965) introduced the essential approximation that allows channeling to be analyzed, the approximation of using potentials and atomic and electronic distributions averaged along the channeling direction. With this approximation longitudinal and transverse

variables may be separated. The particle moves longitudinally with a slow deceleration determined by the rate of energy loss, while the transverse motion is, ideally, an oscillation within the channel space. In actuality, small nonzero angles of incidence of the particle with respect to the channel direction, thermal vibration of the crystal atoms, and crystal imperfections and impurities can cause the channeling particle to wander among neighboring channels and to dechannel. (A particle dechannels when it is deflected through a large angle and thereafter does not travel along the channel direction at all.)

Theoretical calculations of channeling energy loss generally divide the energy loss into three parts, each of which can be easily approximated: that due to local electrons, to distant valence electrons, and to core electrons of the crystal atoms. In Section II we summarize a recent version of this theory with brief derivations. Section III gives an analysis of straggling and Section IV the description of a computer program which analyzes trajectories, energy loss, and straggling according to this theory. Results from the computer program are given graphically in several figures.

Section V describes a high resolution experimental system which was set up for taking transmission spectra of protons channeling through thin silicon crystal targets. The results, summarized in VI along with available data in the literature, are precise enough to give values of straggling as well as energy loss.

One part of the theoretically calculated channeling rate of energy loss depends on the local electron distribution within the channels of the crystal. By comparing the experimental data with the theory,

values for the local electron densities in the centers of various channels are obtained. These values and other comparisons between theoretical and experimental energy loss and straggling data are presented and discussed in Section VI.

Energy loss of molecular ions has also been examined theoretically and experimentally in an attempt to determine if there is any difference from the atomic case. Some theoretical arguments suggest that for a few channeling H_2^+ and H_3^+ molecules, after they enter the crystal and are dissociated, two of the protons channel through together resulting in a reduced energy loss. Experiments carried out to look for differences between atomic and molecular energy loss are described in Section VII. They gave no evidence of any difference.

II. THEORY OF ENERGY LOSS

We follow the theory developed in Appleton, Erginsoy, and Gibson (1967) and Luntz and Bartram (1968). We will be concerned with low mass ions of energies greater than or equal to 500 KeV. For such ions the trajectory of the motion is determined mostly by ion-crystal atom nuclei interactions and the energy loss is dominated by ion-crystal atom electron interactions.

Express the ion-nucleus interaction by the Molière approximation to the Thomas Fermi potential:

$$V(r) = \frac{Z_{ion} Z\, e^2}{r} \left(0.1\, e^{-6r/a_{tf}} + 0.55\, e^{-1.2r/a_{tf}} + 0.35\, e^{-.3r/a_{tf}}\right)$$

where

r = distance between the ion and the nucleus

a_{tf} = .8853 x (Bohr radius)/$(Z_{ion}^{2/3} + Z^{2/3})^{1/2}$

Z_{ion} = the average charge in units of e on the ion while it channels through the crystal

Z = the atomic number of the crystal atoms

(Other potentials may be chosen. The potential affects the rate of energy loss in two ways, by determining the trajectory of the channeling ion and by determining the local electron distribution in the channel through Gauss' law.)

The channeling approximation consists of representing the charge distribution in rows or planes of crystal atoms between which the channeling occurs as the uniform charge distribution obtained by

averaging the actual charge distribution. Thus, for axial channeling in the channeling approximation, we have the ion-row interaction

$$V_{ax}(\rho) = \lambda \int_{-\infty}^{\infty} V(\sqrt{\rho^2 + x^2})dx$$

$$= 2Z_{ion}Ze^2 \lambda[0.1K_o(\frac{6\rho}{a_{tf}}) + 0.55K_o(\frac{1.2\rho}{a_{tf}}) + 0.35K_o(\frac{0.3\rho}{a_{tf}})]$$

where

ρ = perpendicular distance from the ion to the row

λ = linear density of atoms in the row

The motion of the ions is governed by the total potential

$$V_{ax,total}(\rho) = \sum_i V_{ax}(|\rho - \rho_i|)$$

where

$|\rho - \rho_i|$ = perpendicular distance from the ion to the i^{th} row

Similarly, for planar channeling we have the ion-plane interaction

$$V_{pl}(y) = n \int_0^{\infty} V(\sqrt{\rho^2 + y^2})\, 2\pi\rho\, d\rho$$

$$= 2\pi n\, Z_{ion}Ze^2\, a_{tf}(\frac{0.1}{6} e^{-6y/a_{tf}}$$

$$+ \frac{0.55}{1.2} e^{-1.2y/a_{tf}} + \frac{0.35}{0.3} e^{-0.3y/a_{tf}})$$

where

y = perpendicular distance from the ion to the plane

n = average density of atoms in the plane

and the motion of the ions is governed by

$$V_{pl,total}(y) = \sum_i V_{pl}(|y - y_i|)$$

where

$|y - y_i|$ = perpendicular distance from the ion to the i^{th} plane

The energy loss of ions channeling in crystals may be divided into three parts which we will describe in the following three subsections. Each of these parts is proportional to Z_{ion}^2. For small ion velocities Roll and Steigert (1960) and others have found that the theoretical value for dE/dx agrees more closely with experiment if Z_{ion} is replaced by a reduced effective charge Z_{ion}^*. We follow Luntz and Bartram and take Z_{ion}^* to be given by

$$Z_{ion}^*(v_{ion}) = Z_{ion}[1 - \exp\{-v_{ion} \times 137/(c \times Z_{ion}^{2/3})\}]$$

A. Energy Loss Due to Local Electrons

Nearby electrons scatter from the passing incident ion with high momentum transfer. Define Q = (momentum transfer to electron)^2/(2m) and take the formula given in U. Fano's review article (1963) for nonrelativistic high Q energy loss

$$-\left.\frac{dE}{dx}\right|_{\text{high Q}} = \int_{Q_{cutoff}}^{Q_{max}} Q \, d\sigma(Q) \qquad (1)$$

$$d\sigma(Q) = \frac{2\pi Z^{*2}_{ion} e^4}{m v^2_{ion}} NZ_1 \frac{dQ}{Q^2} \qquad (2)$$

where

Q_{max} = maximum possible energy transfer to a stationary electron = $2mv^2_{ion}$

v_{ion} = velocity of the ion

N = density of atoms in the crystal

Z_1 = effective number of crystal electrons per atom for high Q interactions

m = mass of the electron

Bohm and Pines' random phase approximation, see for instance Pines (1964), gives a cutoff of

$$Q_{cutoff} = \frac{\hbar^2}{2m} k_c^2$$

where

$$k_c = \omega_{plasma}/v_{Fermi}$$

$$\omega_{plasma} = (4\pi e^2 NZ_{val}/m)^{1/2}$$

(Experimentally determined values for ω_{plasma} are close to this theoretical expression. We use the experimental values in all our numerical calculations.)

$$v_{Fermi} = \hbar(3\pi^2 NZ_{val})^{1/3}/m$$

This equation for Q_{cutoff} implies that the high Q interactions occur with electrons right along the ion's path: The Born approximation for the energy transferred to a stationary electron by a passing ion of energy E_{ion} and impact parameter b is

$$\frac{Z^{*2}_{ion}\, e^4 M}{m E_{ion}\, b^2}$$

where

M = mass of the proton

This quantity equals Q by the definition of Q . $Q > Q_{cutoff}$ yields the equation

$$b < b_{max} = \frac{Z^{*}_{ion}\, e^2 v_{Fermi}}{\hbar\omega_{plasma}} \sqrt{\frac{2M}{E_{ion}}}$$

which, for protons channeling in silicon, becomes $b_{max} = .261\text{Å}/\sqrt{E_{ion}(\text{in MeV})}$. In the range $E_{ion} > .5$ MeV of interest to us, b_{max} is considerably less than the sizes of low index channels. Therefore we may equate Z_1 to the number of electrons per crystal atom along the ion's trajectory, Z_{loc} .

The above statements combine to give

$$-\left.\frac{dE}{dx}\right|_{local} = \frac{4\pi Z^{*2}_{ion}\, e^4}{m v^2_{ion}} N Z_{loc}\, \ell n\, \frac{2 m v_{ion} v_{Fermi}}{\hbar\omega_{plasma}} \qquad (3)$$

B. Energy Loss Due to Resonant Interactions with Distant Electrons

Loosely bound distant electrons in a crystal (the "valence" electrons) interact collectively with the passing ion and cause energy loss. Lindhard (1954) has analyzed this process in the approximation of a charged gas for the valence electrons. In terms of the dielectric

constant of the gas, $\varepsilon(k,\omega)$, Lindhard obtains

$$-\left.\frac{dE}{dx}\right|_{resonant} = \int_0^\infty p(\omega)\,\hbar\omega\,d\omega \tag{4}$$

where

$p(\omega)$ =(probability of energy loss $E = \hbar\omega$) / (distance traveled)

$$= \int_0^\infty \frac{Z_{ion}^{*2}\, e^2}{\hbar\pi v_{ion}^2} \times \mathrm{Im}\left(\frac{1}{\varepsilon(k,\omega)} - \frac{1}{\varepsilon(k,-\omega)}\right)$$

$$\times\, H(kv_{ion} - \omega)\,\frac{dk}{k} \tag{5}$$

and

$$\varepsilon(k,\omega) = 1 + \frac{\omega_{plasma}^2}{(\hbar k^2/2m)^2 - (\omega + i\gamma)^2}$$

$$\omega_{plasma}^2 = 4\pi e^2 N Z_{val}/m$$

γ infinitesimal and positive

$$H(x) = \begin{cases} 1, & x \geq 0 \\ 0, & x \leq 0 \end{cases}$$

Z_{val} = number of valence electrons per crystal atom

We cut off the k integral above at the Bohm and Pines limit, $k_c = \omega_{plasma}/v_{Fermi}$ (see subsection A above). For $2mv_{ion}^2 >> \hbar\omega_{plasma}$ and $2mv_{ion}v_{Fermi} > \hbar\omega_{plasma}$ (which are approximations that hold for protons channeling in silicon or germanium with energies greater than 500 KeV) we obtain

$$\left.\frac{dE}{dx}\right|_{resonant} = \frac{4\pi Z^{*2}_{ion}\, e^4}{m v^2_{ion}} N Z_{val}\, \ell n\, \frac{v_{ion}}{v_{Fermi}} \qquad (6)$$

C. Energy Loss Due to Core Electrons

As was stated in subsection A, the Born approximation for the energy lost to a stationary electron by a passing ion of impact parameter b is

$$\delta E(b) = \frac{2Z^{*2}_{ion}\, e^4}{m v^2_{ion}} \frac{1}{b^2} \qquad (7)$$

The energy loss due to core electrons of crystal atoms is

$$\left.\frac{dE}{dx}\right|_{core} = \sum_{ij} c_i\, \sigma_j\, \delta E(b_j) \qquad (8)$$

where

σ_j = atomic density of row or plane j

b_j = impact parameter of the ion with respect to row or plane j

c_i = number of electrons/atom in core electron shell i

The sum over j is over all atoms in a cylinder with axis along the ion's path, of unit length and radius equal to b_{max} which is given by the standard adiabatic condition

$$b_{max,i} = \frac{\hbar v_{ion}}{\Delta E_i}$$

ΔE_i = ionization energy of electrons in core electron shell i

For axial channeling

$$-\left.\frac{dE}{dx}\right|_{core} = \frac{2Z^{*2}_{ion}\, e^4}{mv^2_{ion}} \sum_i \sum_j c_i \lambda_j \frac{1}{|\rho - \rho_j|^2} \tag{9}$$

where

c_i = number of electrons in shell i of the crystal atoms

λ_j = linear density of atoms in row j

and, for each i, the sum is over all j such that

$$|\rho - \rho_j| \leq \hbar v_{ion}/\Delta E_i$$

For planar channeling

$$-\left.\frac{dE}{dx}\right|_{core} = \frac{2Z^{*2}_{ion} e^4}{mv^2_{ion}} \sum_i \sum_j c_i n_j \int_{-a_{ij}}^{a_{ij}} \frac{dx}{x^2 + |y - y_j|^2} \tag{10}$$

where

$$a_{ij} = \begin{cases} [(\hbar v_{ion}/\Delta E_i)^2 - |y - y_j|^2]^{1/2}, & \text{if this value is real} \\ 0, & \text{otherwise} \end{cases}$$

n_j = planar density of atoms in plane j

Carry out the integration:

$$-\left.\frac{dE}{dx}\right|_{core} = \frac{2Z^{*2}_{ion}\, e^4}{mv^2_{ion}} \sum_i \sum_j c_i n_j \frac{1}{|y - y_j|} \times 2 \arctan\left[\left(\frac{\hbar v_{ion}}{\Delta E_i |y - y_j|}\right)^2 - 1\right]^{1/2} \tag{11}$$

D. Summary

The total rate of energy loss for an ion traveling through a crystal is the sum of the three contributions above (equations (3), (6), and (9) or (11)):

$$-\frac{dE}{dx} = \frac{2Z_{ion}^{*2}\, e^4}{mv_{ion}^2}\left[2\pi N\left(Z_{loc}\ \ell n\ \frac{2mv_{ion}\, v_{Fermi}}{\hbar\,\omega_{plasma}} + Z_{val}\ \ell n\ \frac{v_{ion}}{v_{Fermi}}\right)\right. \tag{12}$$

$$\left. + \sum_i c_i \begin{cases} \sum_j{}' \dfrac{\lambda_j}{|\rho - \rho_j|^2} \Big] , & \text{for axial channeling} \\ \sum_j{}' n_j \dfrac{2 \arctan w_{ij}}{|y - y_j|} \Big] , & \text{for planar channeling} \end{cases}\right.$$

where

$$w_{ij} = \left[\left(\frac{\hbar v_{ion}}{\Delta E_i\ |y - y_j|}\right)^2 - 1\right]^{1/2}$$

$\sum_j{}'$ is the sum over all j such that $|\rho - \rho_j|$ or $|y - y_j| \leq \hbar\, v_{ion}/\Delta E_i$

The only quantities in this energy loss formula which depend on the channeling direction are Z_{loc}, λ_j or n_j, and ρ_j or y_j.

E. Numerical Example

Consider the case of protons channeling in silicon:

$Z = 14$

$Z_{val} = 4$

$N = 4.915 \times 10^{22} \text{atoms/cm}^3$

$\hbar\omega_{plasma} = 16.6 \text{ eV}$

$c_1 = 6$

$\Delta E_1 = 108.22 \text{ eV}$. Other ΔE_i are larger.

$v_{Fermi} = 2.08 \times 10^8 \text{cm/sec}$

Substitute into equation (12) with $Z^*_{ion} = Z_{ion}$ for simplicity. Then

$$-\frac{dE}{dx} = 1175 \frac{\text{Kev}}{\mu\text{m}} \quad \frac{2.98\, Z_{loc} + 7.59 + (\frac{1}{2} Z_{loc} + 2)\, \ell n\, E}{E}$$

$$+ \text{(core contributions)}$$

where E is in units of MeV. Core contributions are present when

$$E > E_{min} = 1.41 \text{ MeV } \rho^2$$

where ρ is the distance in $\mathring{A}$ from the channel to the nearest plane or row of crystal atoms. Table 1 gives ρ and E_{min} values for common channels in silicon.

Table 1

Widths and minimum energies at which core electrons contribute to energy loss of channeling protons for various low index axial and planar channels in silicon.

Table 1

Channel	ρ = distance to nearest plane or row in Å	E_{min} = minimum energy for core electron contributions in MeV
<100>	1.365	2.63
<110>	2.048	5.91
<111>	1.287	2.34
<211>	1.526	3.28
{100}	.683	.66
{110}	.965	1.31
{111}	1.182	1.97
{211}	.557	.44

III. THEORY OF STRAGGLING

Straggling, the broadening of the energy spectrum of a beam of ions during transmission through a target, is due to two causes: (1) statistical fluctuations in the amount of energy a particle loses while traveling along a given path, and (2) differences in energy loss due to variation in path through the target for different particles in the beam.

A. Straggling Due to Statistical Fluctuations

If N events contribute to energy loss, a fractional standard deviation in the value of the energy loss of order $N^{-1/2}$ is expected. More precisely, if

$$-\frac{dE}{dx} = \sum_i \sigma_i \, \delta E_i$$

where

σ_i = cross section for process i

δE_i = energy loss for process i

then

$$\frac{d(\Delta E)^2}{dx} = (\text{standard deviation of the spreading in the energy spectrum})^2/(\text{distance through target})$$

$$= \sum_i \sigma_i \, \delta E_i^2$$

From the formula for energy loss due to local electrons, equations (1) and (2), we obtain

$$\left.\frac{d(\Delta E)^2}{dx}\right|_{local} = \int_{\frac{\hbar^2}{2m}\frac{\omega_{plasma}^2}{v_{Fermi}^2}}^{2mv_{ion}^2} \frac{2\pi Z_{ion}^{*2} e^4}{mv_{ion}^2} NZ_{loc} \frac{dQ}{Q^2} Q^2$$

$$= \frac{2\pi Z_{ion}^{*2} e^4}{mv_{ion}^2} NZ_{loc}\left(2mv_{ion}^2 - \frac{\hbar^2}{2m}\frac{\omega_{plasma}^2}{v_{Fermi}^2}\right)$$

From the formula for energy loss due to resonant interactions with distant electrons, equations (4) and (5), we obtain

$$\left.\frac{d(\Delta E)^2}{dx}\right|_{resonant} = \int_0^\infty p(\omega)\ (\hbar\omega)^2\ d\omega$$

$$= \int_0^{\omega_{plasma}/v_{Fermi}} \frac{dk}{k}$$

$$\times \int_0^{kv_{ion}} \frac{Z_{ion}^{*2} e^2}{\hbar\pi v_{ion}^2} \times \mathrm{Im}\left(\frac{1}{\varepsilon(k,\omega)} - \frac{1}{\varepsilon(k,-\omega)}\right)(\hbar\omega)^2\ d\omega$$

As before, we assume the approximation $2mv_{ion}^2 >> \hbar\omega_{plasma}$ and $2mv_{ion}v_{Fermi} > \hbar\omega_{plasma}$. Note that $2mv_{Fermi}^2 > \hbar\omega_{plasma}$, and that for energies of interest to us, $\ell n(v_{ion}/v_{Fermi}) < 4$. Then we may integrate $d(\Delta E)^2/dx$ to obtain the inequality $d(\Delta E)^2/dx < 4\pi Z_{ion}^{*2} e^4 NZ_{val}$ $(4\sqrt{2}\ \hbar\omega_{plasma})/(mv_{ion}^2)$.

If this is added to the local electron $d(\Delta E)^2/dx$ expression above, we are left with (in the approximation described)

$$\left.\frac{d(\Delta E)^2}{dx}\right|_{\substack{\text{local and}\\ \text{resonant}}} = 4\pi Z_{ion}^{*2}\, e^4\, NZ_{loc} \tag{13}$$

Finally, we examine core electron contributions. In the axial channeling case we obtain from equations (7), (8), and (9)

$$\left.\frac{d(\Delta E)^2}{dx}\right|_{\substack{\text{core}\\ \text{axial}}} = \left(\frac{2Z_{ion}^{*2}\, e^4}{mv_{ion}^2}\right)^2 \sum_i \sum_j{}' \frac{c_i \lambda_j}{|\rho - \rho_j|^4} \tag{14}$$

The meaning of $\sum_j{}'$ is given above following equation (12). In the planar channeling case we obtain from equations (7), (8), and (10)

$$\left.\frac{d(\Delta E)^2}{dx}\right|_{\substack{\text{core}\\ \text{planar}}} = \left(\frac{2Z_{ion}^{*2}\, e^4}{mv_{ion}^2}\right)^2 \sum_i \sum_j{}' c_i n_j$$

$$\cdot \int_{-a_{ij}}^{a_{ij}} \frac{dx}{(x^2 + |y - y_j|^2)^2}$$

$$= \left(\frac{2Z_{ion}^{*2}\, e^4}{mv_{ion}^2}\right)^2 \sum_i \sum_j{}' \frac{c_i n_j}{|y - y_j|^3} \left(\arctan w_{ij} + \frac{w_{ij}}{w_{ij}^2 + 1}\right) \tag{15}$$

where

$$w_{ij} = \frac{a_{ij}}{|y - y_j|} = \left[\left(\frac{\hbar v_{ion}}{\Delta E_i |y - y_j|}\right)^2 - 1\right]^{1/2}$$

B. Straggling Due to Variation in Path Through the Target

Choose a particular axial (or planar) channeling direction in the crystal (k_1,k_2,k_3). The variable $\underset{\sim}{\rho}$ (or y) in the basic energy loss formula (12) designates which of the many possible paths parallel to the (k_1,k_2,k_3) axes (between the (k_1,k_2,k_3) planes) the ion takes. Let us define a channel as any such path along which the ion's energy loss is minimized. Choose a particular channel and choose coordinates so that $\underset{\sim}{\rho}$ (or y) is zero along the channel.

When an ion channels, it either travels right along a channel or makes small oscillations about a channel. Therefore, to first order

$$-\frac{dE}{dx} \sim A(E) + B(E) \times (\text{distance from channel})^2 \qquad (16)$$

where A and B are positive functions of energy. In the case of axial channeling, perpendicular components ρ_x and ρ_y of $\underset{\sim}{\rho}$ can be found so that

$$-\frac{dE}{dx} = A + B_x(E)\,\rho_x^2 + B_y(E)\,\rho_y^2$$

If we average over angle in the plane of $\underset{\sim}{\rho}$ we obtain

$$-\frac{dE}{dx} = A(E) + B(E)\,\rho^2$$

where

$$B = \frac{1}{2}(B_x + B_y)$$

$$\rho = (\rho_x^2 + \rho_y^2)^{1/2} = |\underset{\sim}{\rho}|$$

In the case of planar channeling we have

$$-\frac{dE}{dx} = A(E) + B(E)\, y^2$$

Consider a beam of ions of energy E_{in} entering the crystal target at a small angle θ with respect to the channel direction. (This angle will be referred to as the incidence angle.) As the particle passes through the crystal target we expect ρ or y to vary approximately as

$$C(E)\ \theta\ \sin[\omega(E)t]$$

where

t = time

$C(E)$ = (the amplitude of oscillation about the channel for beam of energy E) / θ

$\omega(E)$ = the frequency of oscillation

Assume that we know $E(t)$, the energy of the particle while passing through the target, as a function of time. In the cases of interest to us, A, B, C, and ω vary slowly with energy as compared to the rate of oscillation of $\sin[\omega t]$ so that we may take time averages:

$$\langle B(E)\ C(E)^2\ \theta^2 \sin^2[\omega(E)t] \rangle_t = \frac{1}{2} B(E)\ C^2(E)\ \theta^2$$

$$-\left\langle \frac{dE}{dx} \right\rangle_t = A(E) + \frac{1}{2} B(E)\ \theta^2\ C^2(E)$$

If the target thickness is Δx, the total energy lost by particles of

incidence angle θ is

$$\Delta E_\theta = \int_0^{\Delta x} A(E)\, dx + \frac{\theta^2}{2} \int_0^{\Delta x} B(E)\, C^2(E)\, dx$$

Let ΔE_θ be small. Then A and B are approximately functions of E_{in} only. (We shall say that the target is <u>thin</u> in this case.) ΔE_θ will be given by

$$[A'(E_{in}) + B'(E_{in})\theta^2]\ \Delta x$$

where $A' = A$ and $B' = B \times C^2/2$, and in the limit $\Delta x \to 0$ we may write

$$-\left.\frac{dE}{dx}\right|_\theta = A'(E) + B'(E)\ \theta^2$$

Consider a beam of particles of energy E_{in} and half angular divergence ϕ incident along the channel direction. For any angle $\theta < \phi$, the fraction of the beam $2\pi\theta\, d\theta/(\pi\phi^2) = 2\theta d\theta/\phi^2$ enters the target with incident angle between θ and $\theta + d\theta$. Incidence angle θ corresponds to energy loss $-\Delta E_\theta = [A'(E_{in}) + B'(E_{in})\theta^2]\ \Delta x$ in a thin target. Therefore the energy spectrum of particles coming out of the target is

$$\begin{cases} \dfrac{2\theta(E)}{\phi^2}\ \dfrac{d\theta(E)}{dE}\, dE & \text{, if } E_{in} - A'\Delta x \geq E \geq E_{in} - (A' + B'\phi^2)\ \Delta x \\ 0 & \text{, otherwise} \end{cases}$$

where $\theta(E)$ is the positive solution of $E = E_{in} - \Delta E_{\theta(E)}$. If we differentiate $E = E_{in} - \Delta E_{\theta(E)}$, we obtain

$$dE = d(-\Delta E_{\theta(E)}) = d[A' + B'\theta^2(E)]\,\Delta x$$

$$= B'(E_{in})\, 2\theta(E)\, d\theta(E)\, \Delta x$$

Thus we find that we have a square energy spectrum, zero outside of $E_{in} - A'\,\Delta x \geq E \geq E_{in} - (A' + B'\phi^2)\Delta x$, and equal to a constant inside this interval. The endpoints of this interval are equal to

$$E - \Delta E\big|_{\theta=0} \quad \text{and} \quad E - \Delta E\big|_{\theta=\phi}$$

The <u>full width</u> of the straggling in this case is therefore given by

$$w = \Delta E\big|_{\theta=\phi} - \Delta E\big|_{\theta=0} = B'\phi^2\,\Delta x \tag{17}$$

Recall that $B' = B(E_{in})\, C^2(E_{in})/2$. From equation (12) we see that there are two additive contributions to B. One is from second order variation in Z_{loc} and the other from second order variation in the core contribution to dE/dx with distance ρ (or y) from the channel. Since we are interested in extracting the local electron densities of crystal targets by fitting data with the theory, let us examine the first of these contributions to B'.

Assume that Z_{loc} is minimum along the channel. This is reasonable from crystal symmetry considerations. Z_{loc} may be written to second order in ρ (or y) as, in the axial channeling case,

$$Z_{loc}(\underset{\sim}{\rho}) = Z_{loc}^{(0)} + Z_{loc}^{(2x)}\rho_x^2$$

$$+ Z_{loc}^{(2y)}\rho_y^2$$

$$= Z_{loc}^{(0)} + Z_{loc}^{(2)} \rho^2 \quad \text{(after averaging over direction in the plane of } \underset{\sim}{\rho}\text{)}$$

where

$$Z_{loc}^{(2)} = \frac{1}{2}\left(Z_{loc}^{(2x)} + Z_{loc}^{(2y)}\right)$$

For planar channeling we may write

$$Z_{loc}(y) = Z_{loc}^{(0)} + Z_{loc}^{(2)} y^2$$

In both cases $Z_{loc}^{(2)}$ is a nonnegative number with units $1/(\text{distance})^2$. If we compare equations (12), (16), and the above equations for Z_{loc}, and use $B(E) = B(E)\, C^2(E)/2$ we see that

$$B'(E_{in}) = B_1'(E_{in}) Z_{loc}^{(2)} + B_2'(E_{in}) \tag{18}$$

where $B_2'(E_{in})$ is independent of $Z_{loc}^{(2)}$ and comes entirely from core contributions, and B_1' is given by

$$B_1'(E_{in}) = \frac{4\pi Z_{ion}^{*2} e^4}{m v_{ion}^2} N \ln\left(\frac{2m v_{ion} v_{Fermi}}{\hbar \omega_{plasma}}\right) \frac{C^2(E_{in})}{2}$$

We may estimate $C(E_{in})$ in terms of the distance ρ_o (or y_o) to the nearest row (or plane) of crystal atoms and the maximum angle of incidence $\Phi_{max}(E_{in})$ for which channeling occurs:

$$C(E_{in}) \cong \frac{\rho_o (\text{ or } y_o)}{\psi_{max}(E_{in})}$$

Thus we have

$$B_1'(E_{in}) = \frac{2\pi Z_{ion}^{*2} e^4}{mv_{ion}^2} \frac{N\rho_o^2(\text{or } y_o^2)}{\psi_{max}^2(E_{in})} \ell n \frac{2mv_{ion}v_{Fermi}}{\hbar \omega_{plasma}} \tag{19}$$

In the limit of many particles passing through an infinitely thin target we may write equations (17) and (18) in the form

$$\frac{dw}{dx} = B'(E_{in})\phi^2 = [B_1'(E_{in})Z_{loc}^{(2)} + B_2'(E_{in})]\,\phi^2 \tag{20}$$

$$= -\left.\frac{dE}{dx}\right|_{\theta=\phi} + \left.\frac{dE}{dx}\right|_{\theta=0} \tag{21}$$

To convert from our full width of the straggling w to the more usual measure of width, standard deviation σ, note that a square distribution of width w has standard deviation

$$\sigma = \frac{1}{2\sqrt{3}}\, w \tag{22}$$

Our discussion of a beam entering a crystal exactly in the center of a channel with some specified angular divergence is hypothetical, but the results of this discussion can be easily converted to approximate the real situation.

In the real situation, beam particles enter the crystal both near and far from centers of channels. Let a given incident particle have impact parameter b with respect to the channel. Since the row or plane averaged crystal potential V is minimum at the channel's center, the particle will experience a force which bends its trajectory.

The resulting trajectory will oscillate about the channel's center. In the case of a particle entering the crystal parallel to the channel direction, its trajectory will eventually intersect the channel center line. Let θ be the angle of intersection. In the approximation of a quadratic potential V, the angle θ will be proportional to b and an incident beam of many parallel particles will travel along trajectories for which the distribution of angles θ will be the same as that for a beam of half angular divergence ψ_{max} entering at the center of the channel. Thus equation (19) applies with $\phi = \psi_{max}$ and we obtain from equations (20) and (21)

$$\frac{dw}{dx} \cong -\left.\frac{dE}{dx}\right|_{\theta=\psi_{max}} + \left.\frac{dE}{dx}\right|_{\theta=0}$$

$$\cong \frac{2\pi Z_{ion}^{*2} e^4}{mv_{ion}^2} N\rho_o^2(\text{or } y_o^2) Z_{loc}^{(2)} \ell n \frac{2mv_{ion}v_{Fermi}}{\hbar\,\omega_{plasma}}$$

$$+ (\text{core contributions}) \qquad (23)$$

Actual row and plane averaged potentials increase faster than quadratically as one moves away from the channel center (see Appendix A). This will cause the distribution of trajectory angles θ to be more heavily weighted for small angles. The net effect of the non-quadratic part of V on the path variation straggling distribution will be to lower the high energy loss side of the rectangular distribution described above, causing

$$w > 2\sqrt{3}\,\sigma \qquad (24)$$

C. Summary

$d(\Delta E)^2/dx$, the rate of increase of the standard deviation squared of the Gaussian distribution which gives beam energy spectrum spreading due to statistical fluctuations in energy loss events while passing through a target is given in equations (13), (14), and (15).

dw/dx, the rate of increase of the full width of the approximately square distribution which gives beam energy spectrum spreading due to variation of path through a target is given in equation (23).

The energy spectrum of the beam leaving a target is the folding (or convolution) of all distributions representing spreading of the energy spectrum during passage through the target with the incoming beam energy spectrum. It is straightforward to verify that the standard deviation of a convolution of functions is the square root of the sum of squares of the standard deviations of each function. Thus, an incoming beam with energy spectrum having standard deviation σ_{in} leaves the target with spectrum having standard deviation σ_{out} given by $(\Delta E = [d(\Delta E)^2/dx \times \text{target thickness}]^{1/2})$

$$\sigma_{out} = \left[\sigma_{in}^2 + (\Delta E)^2\Big|_{\substack{\text{local and}\\ \text{resonant}}} + (\Delta E)^2\Big|_{\text{core}} + \frac{w^2}{k}\right]^{1/2} \qquad (25)$$

where, by equations (22) and (24), $k = 12$ if the row or plane averaged potential is quadratic and $k > 12$ if the potential increases faster than quadratically away from the channel center.

When w is much larger than ΔE the leading edge of the observed spectrum will be a step function convoluted with a Gaussian.

This leading edge will fall to zero in a manner similar to a Gaussian distribution. Let E_1 be the energy of the point of inflection of the spectrum and let E_2 be the x axis intercept of the tangent line at this point of inflection. Point E_2 will be called the extrapolated leading edge of the spectrum. It is straightforward to verify that

$$E_2 - E_1 = \sqrt{\pi/2}\ \Delta E \cong 1.25\ \Delta E$$

If the incident beam has an energy spread of standard deviation σ_{in} then the discussion above demonstrates that

$$\Delta E = [2(E_2 - E_1)^2 / \pi - \sigma_{in}^2]^{1/2} \tag{26}$$

D. Numerical Example

Refer to the numerical example in subsection IIE above. Consider protons channeling in the <111> direction in silicon. Assume that there are no core electron contributions. $\rho_o = 1.286\text{Å}$. From equation (13)

$$\left.\frac{d(\Delta E)^2}{dx}\right|_{\substack{\text{local and}\\ \text{resonant}}} = 4\pi Z_{ion}^{*2}\, e^4 N Z_{loc} \tag{27}$$

$$= 4\pi e^4 (4.915 \times 10^{22}/\text{cm}^3) Z_{loc} = 1.281\ Z_{loc}\ \frac{\text{KeV}^2}{\mu\text{m}}$$

From equation (23)

$$\frac{dw}{dx} = \frac{2\pi Z_{ion}^{*2} e^4}{mv_{ion}^2} N\rho_o^2 Z_{loc}^{(2)} \ell n \frac{2mv_{ion}v_{Fermi}}{\hbar \omega_{plasma}}$$

$$+ \text{(core contributions)} \qquad (28)$$

$$= .294 \frac{KeV}{\mu m} \frac{5.96 + \ell n\, E}{E} Z_{loc}^{(2)} \rho_o^2 + \text{(core contributions)}$$

where E is the ion's energy in MeV. Let $E = 2$ MeV. Then

$$\frac{dw}{dx} = 1.61 \frac{Kev}{\mu m} Z_{loc}^{(2)} \text{ (in } 1/\mathring{A}^2\text{)}$$

For a target thickness Δx of 1 μm, equations (27) and (28) give $\Delta E \equiv [\Delta x\, d(\Delta E)^2/dx]^{1/2} = 1.13$ KeV Z_{loc}, $w = 1.61$ KeV $Z_{loc}^{(2)}$ (in $1/\mathring{A}^2$). Path variation straggling dominates if $Z_{loc}^{(2)}$ is of the order of Z_{loc} or larger. At lower energies this is true to an even greater extent.

IV. DESCRIPTION OF THE COMPUTER PROGRAM

A computer program has been written which analyzes the geometry of channeling in an arbitrary crystal along an arbitrary direction, and computes energy loss and straggling according to the theory described in Sections II and III. The range of variables that the program was applied to is

$E_{in} \geq .5$ Mev

$Z_{ion} = 1$

Incoming ion = H^+

Target = silicon

Axial orientations: <100> , <110> , <111> , <211>

Planar orientations: {100} , {110} , {111} , {211}

In this section we will describe the computer program and present graphs of its output. The program is subdivided into parts each of which is described in a subsection. The subsection headings summarize the task performed by the part of the program discussed.

A. Determination of the Geometry of the Channeling

When one provides as input:

(a) three vectors which define the sides of a standard cell of the crystal structure,

(b) vectors which give positions of all atoms in the standard

cell, and

(c) the direction of axial or planar channeling,

the program calculates the geometry of the channeling in several initial routines as follows:

1. Axial Channeling. A plane P perpendicular to the axial direction is found. The projection F on this plane of a face of the standard cell, and points of intersection with P of all rows of crystal atoms intersecting F are located. Linear densities for each of these rows of atoms are calculated.

With this information the row averaged Thomas Fermi potential V_{axs} can be computed. Optimal channeling occurs along the trajectory where this potential is minimum. To find the intersection of this minimum trajectory with P the program first locates a likely candidate $\underset{\sim}{x}_0$ as follows: All points $\underset{\sim}{x}$ in P which lie half-way in between the points of intersection with P of some two rows of crystal atoms are found. $\underset{\sim}{x}_0$ is the point $\underset{\sim}{x}$ which lies farthest from any row. Then, starting at $\underset{\sim}{x}_0$, the program applies the path of steepest descent method to find the point in P at which V_{axs} is minimum. This point is taken as the point of intersection of the channel with P.

For crystals and axial directions where the projections on P of the rows of crystal atoms form a pattern of even order rotational symmetry, the channel will necessarily intersect P at a point symmetrical in the sense of $\underset{\sim}{x}_0$. For other orders of symmetry (threefold is common for instance; see Appendix A), all that can be stated

is that x_o probably lies near the channel since it is in a large axial space.

2. Planar Channeling. The spacings between and atomic densities of the planes of crystal atoms in the direction given are computed. The planar channel is located by searching in the largest interplanar space for the minimum of the plane averaged Thomas-Fermi potential.

B. Calculation of Energy Loss

The rate of energy loss is calculated using equation (12) for particles channeling along the center of the channel. For particles incident parallel to the channel direction with impact parameter b with respect to the channel center, the trajectory of the particle is first computed by numerically integrating the transverse equation of motion

$$m_{ion} \frac{d^2\rho}{dt^2} = - Z^*_{ion}\, e \frac{d}{d\rho} V_{Thomas\text{-}Fermi}\ (\rho)$$

(or, for planar channeling, the same equation with y replacing ρ). The resulting motion is oscillatory when d is less than some maximum d_{max} which in turn must be less than the distance ρ_o to the nearest row or plane of crystal atoms. We follow Lindhard (1965) and set $b_{max} = \rho_o - a_{tf}$. When the motion is oscillatory, the program computes the average energy loss rate over one cycle by numerically integrating equation (12) evaluated always at the incoming beam energy. This energy loss rate will be referred to as $dE/dx\big|_b$.

The total energy loss through a target of thickness Δx is obtained by numerically integrating this averaged dE/dx over length Δx .

Graphs of the rate of energy loss in various low index channels of silicon as computed by this part of the program are given in Figure 1.

C. Calculation of Straggling

Statistical straggling is calculated using equations (13) with $Z_{loc} = Z_{loc}^{(0)} + Z_{loc}^{(2)} \rho^2$ (or y^2) , and equations (14) or (15).

Path variation straggling is calculated from

$$\frac{dw}{dx} = - \left.\frac{dE}{dx}\right|_{b_{max}} + \left.\frac{dE}{dx}\right|_{b=0}$$

the impact parameter counterpart of equation (21). (See the discussion at the end of IIIB.)

Figure 1

Calculated values of $dE/dx\big|_{b=0}$ in the energy range 0.5 to 12 MeV for Z_{1oc} = 1,2,3,4, and 5 in low index axial and planar channels of silicon. Vertical dashed lines indicate the onset of various core electron contributions. The labels (k,m) on these dashed lines have the following significance: k labels the electron shell which is beginning to cause additional energy loss. In silicon there are three core electron shells. Herman and Skillman (1963) calculate their energy levels to be

k = 1	$c_1 = 6$	ΔE_1 = 108.22 eV
k = 2	$c_2 = 2$	ΔE_2 = 150.85 eV
k = 3	$c_3 = 2$	ΔE_3 = 1823.72 eV

m = 1,2,··· labels which collection of equidistant rows or planes, in order of increasing distance, the k-shell electrons lie in which are beginning to contribute to dE/dx . Table 1 above gives energies of (1,1) dashed lines, according to this nomenclature.

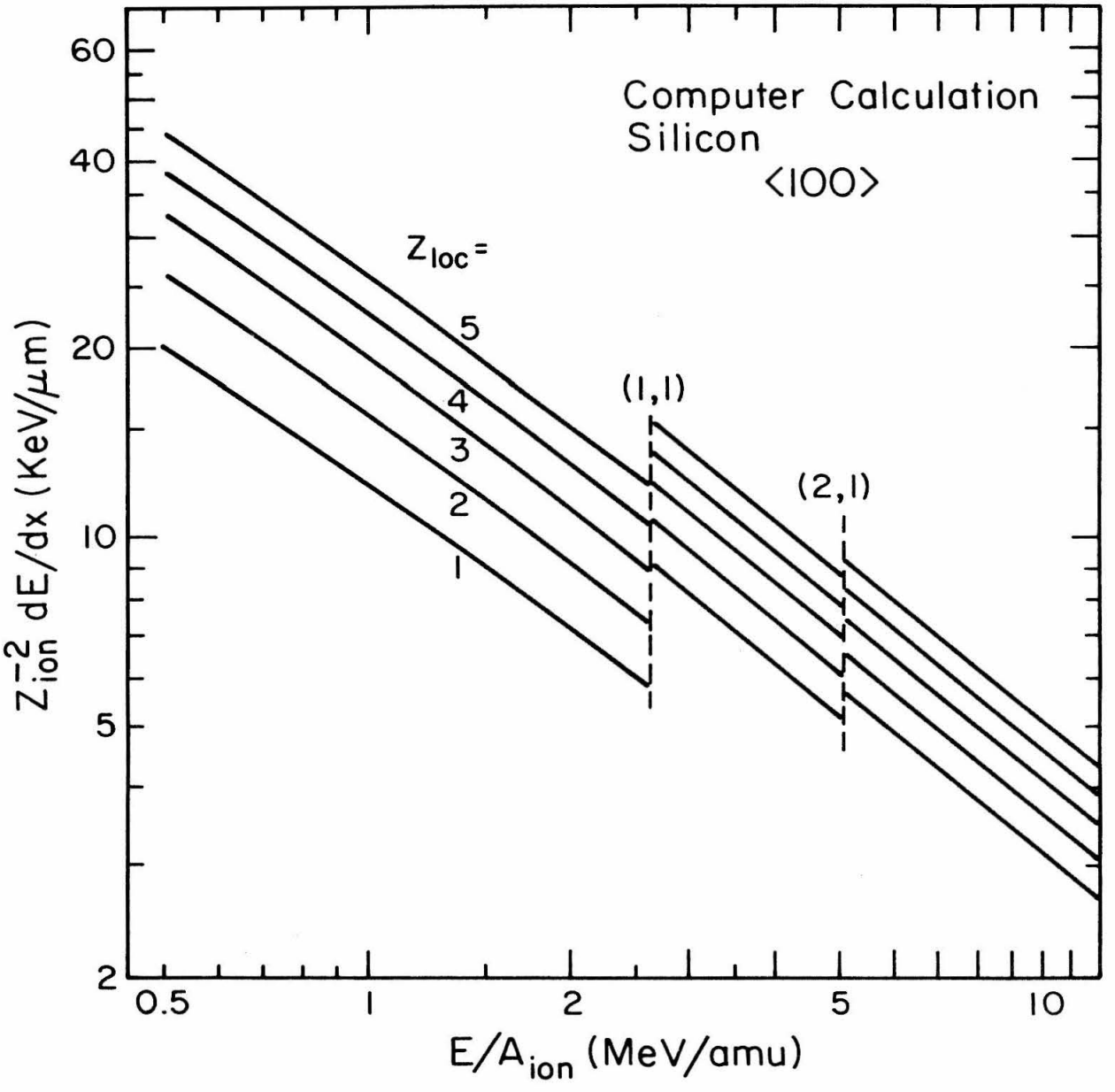
Computer Calculation
Silicon
<100>
Z_{loc} =
5
4
3
2
1
(1,1)
(2,1)
60
40
20
10
5
2
0.5
1
2
5
10
Z_{ion}^{-2} dE/dx (KeV/μm)
E/A_{ion} (MeV/amu)

Figure 1(a)

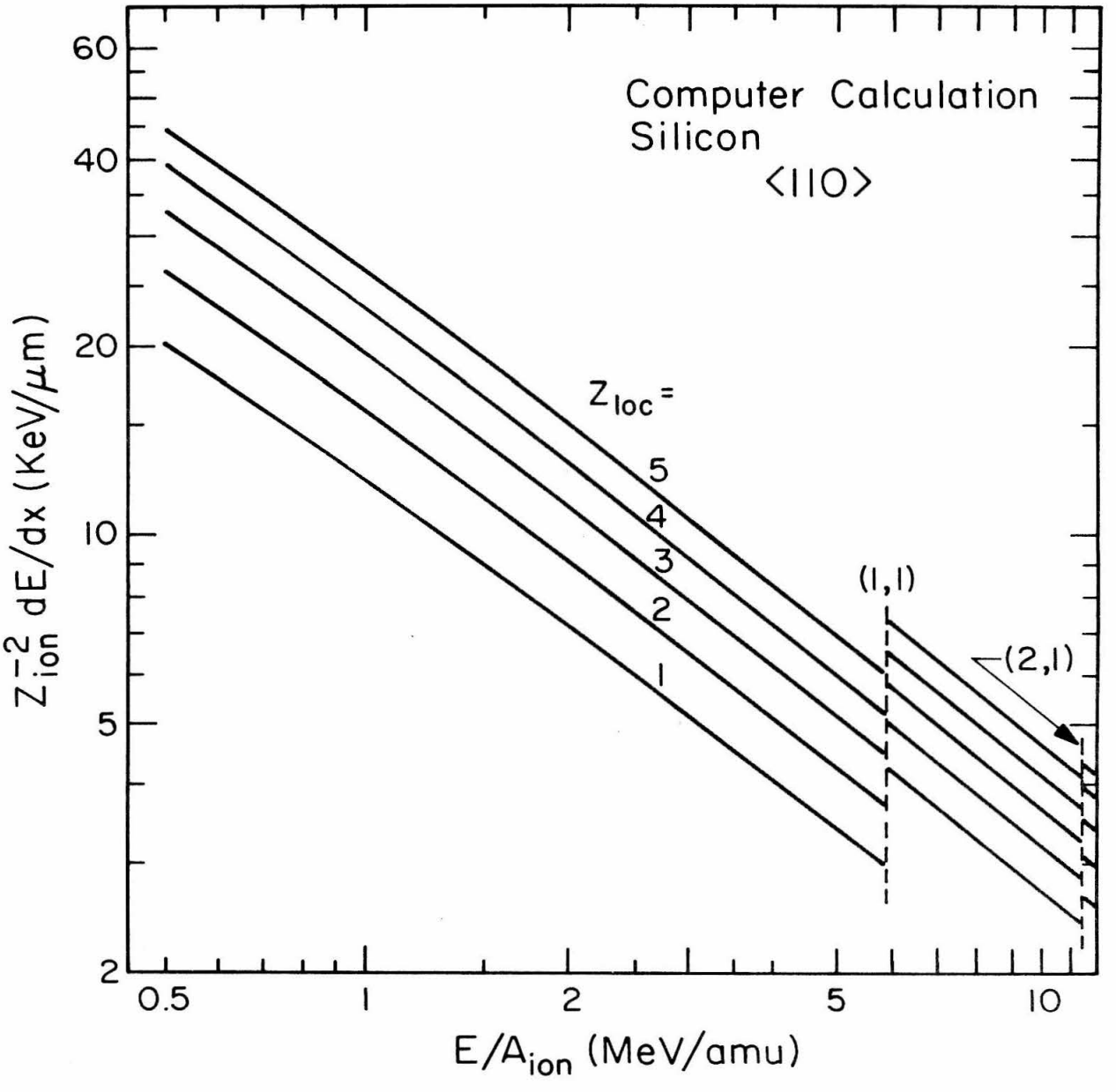
Computer Calculation
Silicon
<110>
Z_{loc} =
5
4
3
2
1
(1,1)
(2,1)
60
40
20
10
5
2
0.5
1
2
5
10
Z_{ion}^{-2} dE/dx (KeV/μm)
E/A_{ion} (MeV/amu)

Figure 1(b)

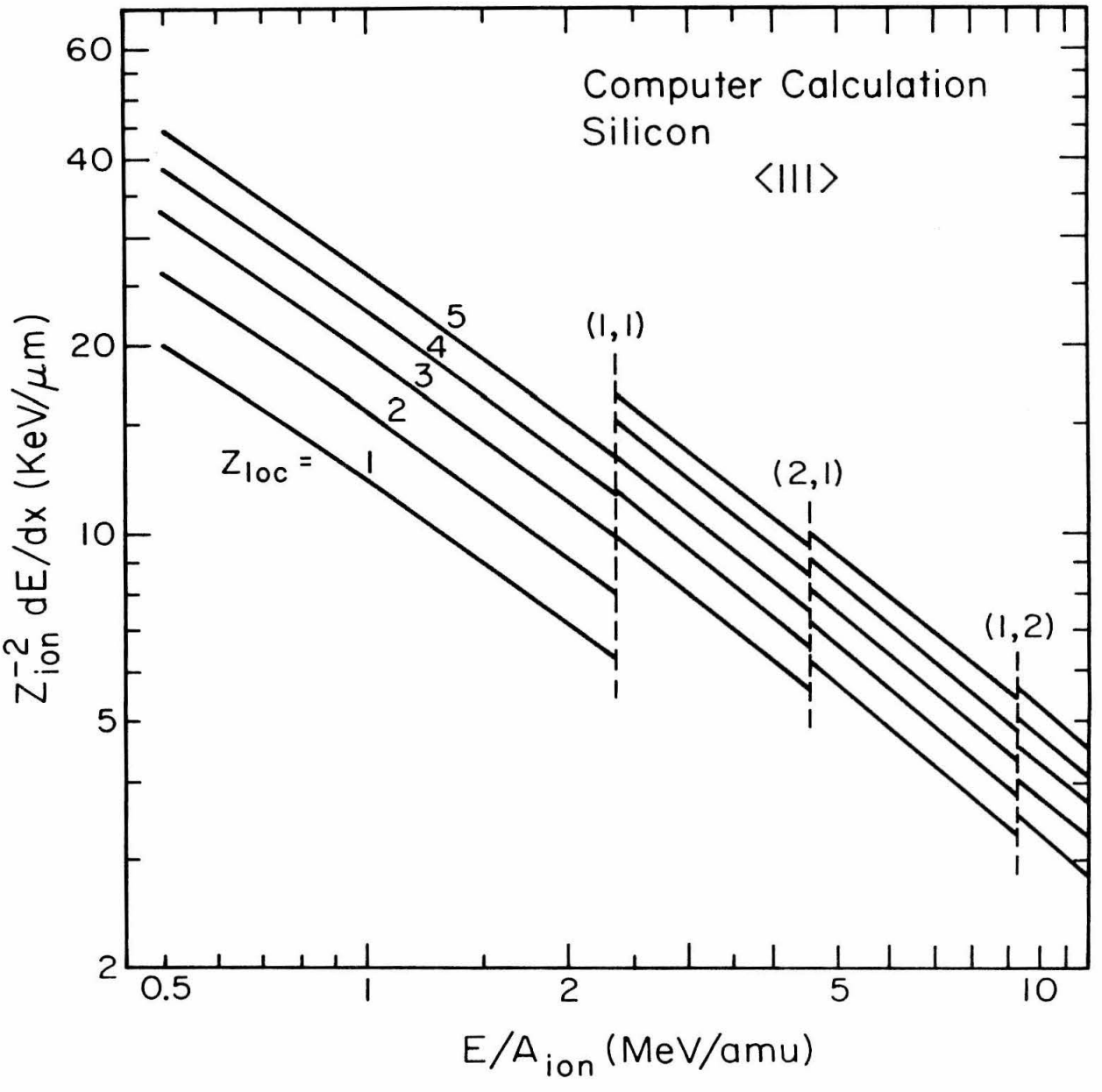
Computer Calculation
Silicon
<111>
(1,1)
(2,1)
(1,2)
Z_{loc} =
5
4
3
2
1
60
40
20
10
5
2
0.5
1
2
5
10
Z_{ion}^{-2} dE/dx (KeV/μm)
E/A_{ion} (MeV/amu)

Figure 1(c)

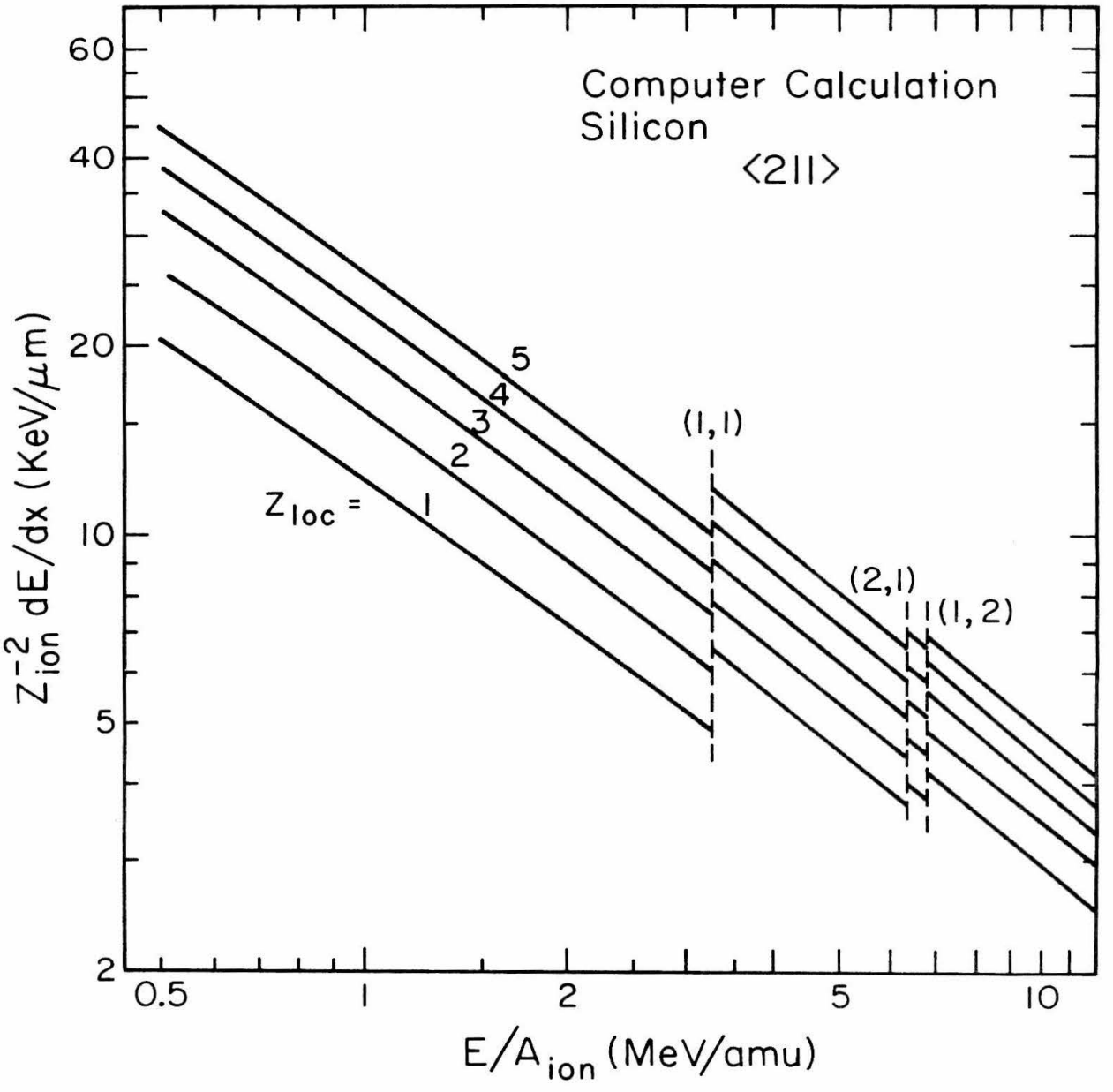
Computer Calculation
Silicon
<211>
60
40
20
10
5
2
0.5
1
2
5
10
5
4
3
2
1
Zloc =
(1,1)
(2,1)
(1,2)
Z_{ion}^{-2} dE/dx (KeV/μm)
E/A_{ion} (MeV/amu)

Figure 1(d)

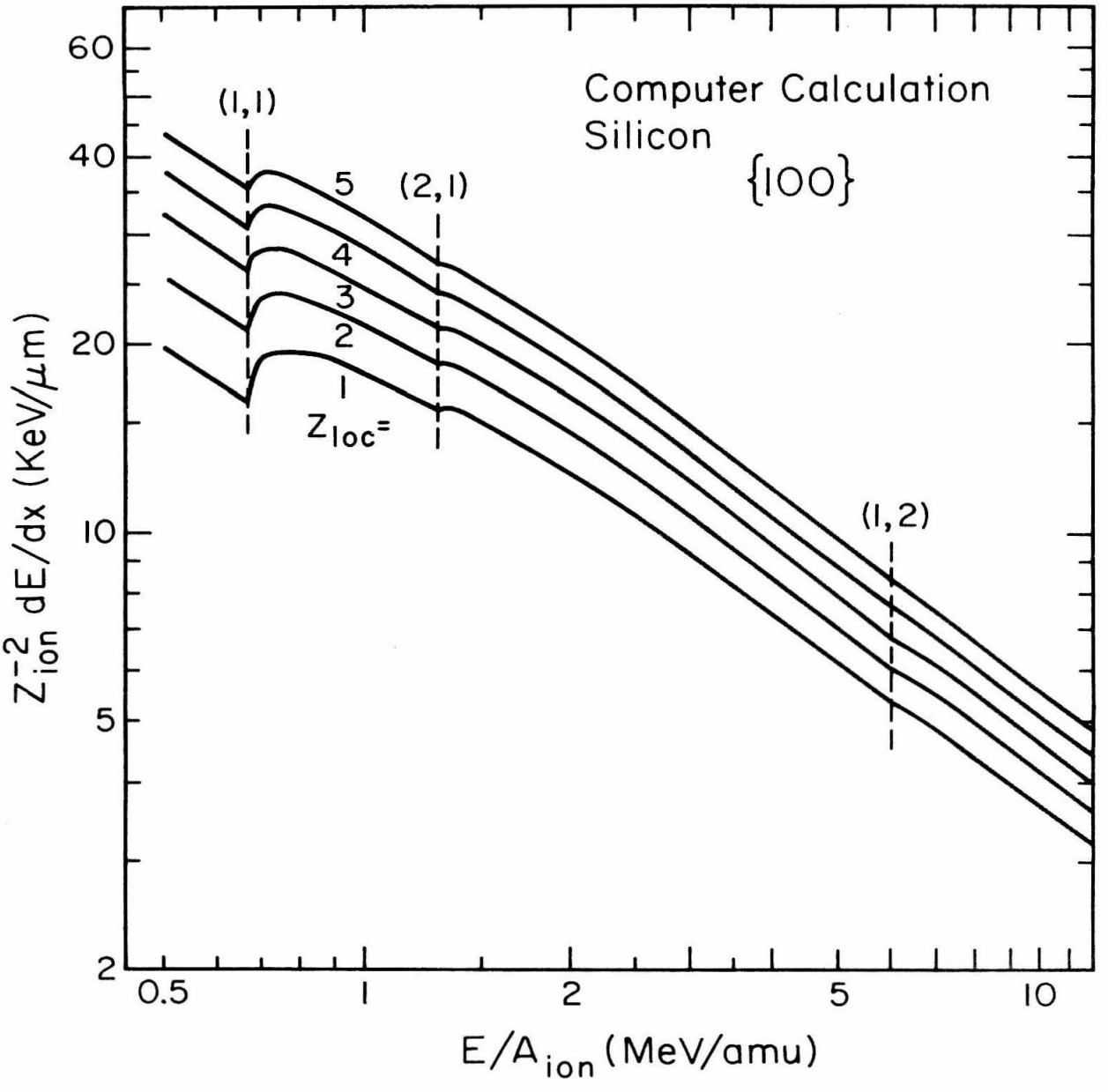
Computer Calculation
Silicon
{100}
(1,1)
(2,1)
(1,2)
5
4
3
2
Z_{loc}=
60
40
20
10
5
2
0.5
1
2
5
10
Z_{ion}^{-2} dE/dx (KeV/μm)
E/A_{ion} (MeV/amu)

Figure 1(e)

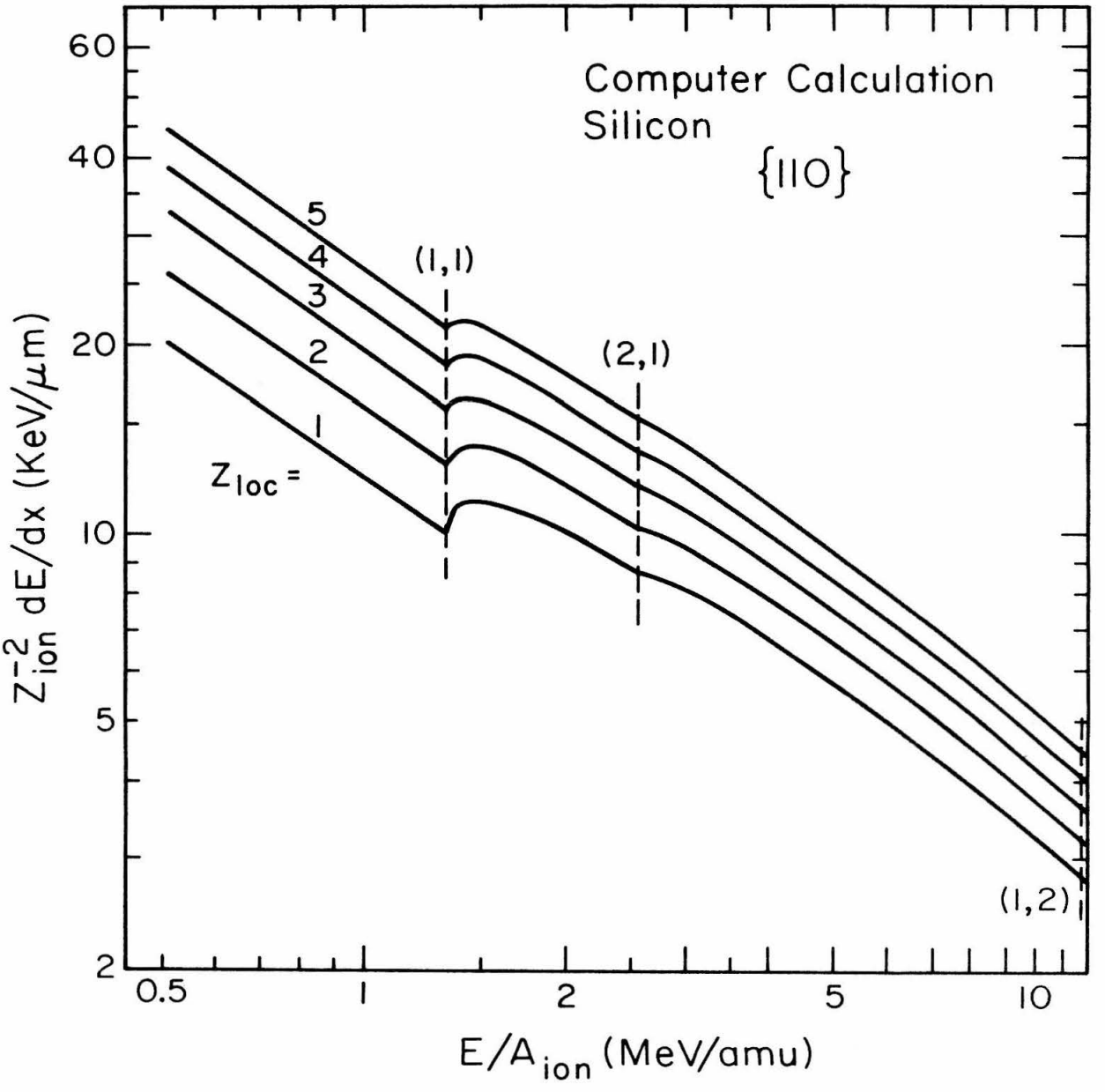

Figure 1(f)

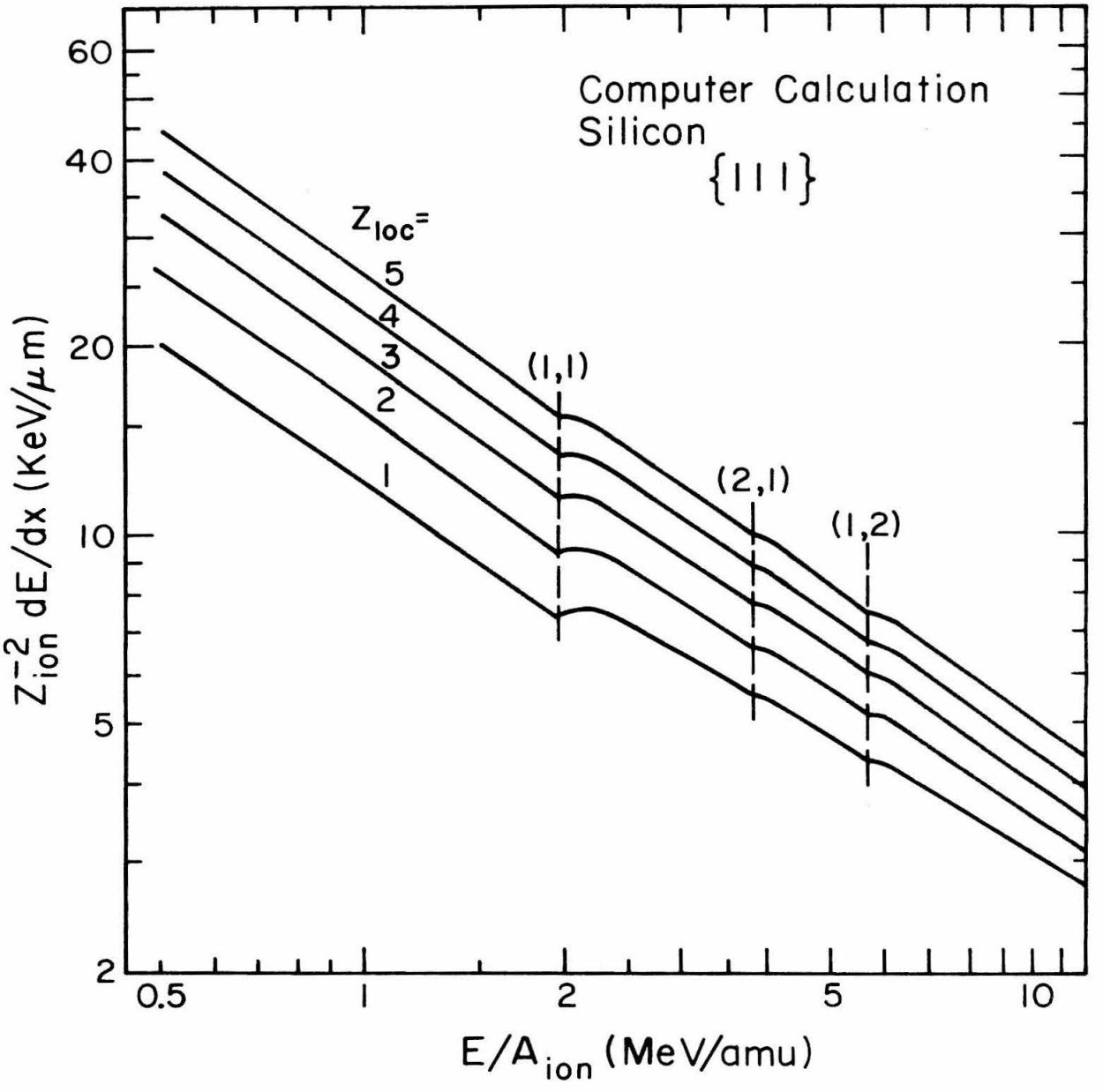
Computer Calculation
Silicon
{111}
Z_{loc}=
5
4
3
2
1
(1,1)
(2,1)
(1,2)
60
40
20
10
5
2
0.5
1
2
5
10
Z_{ion}^{-2} dE/dx (KeV/μm)
E/A_{ion} (MeV/amu)

Figure 1(g)

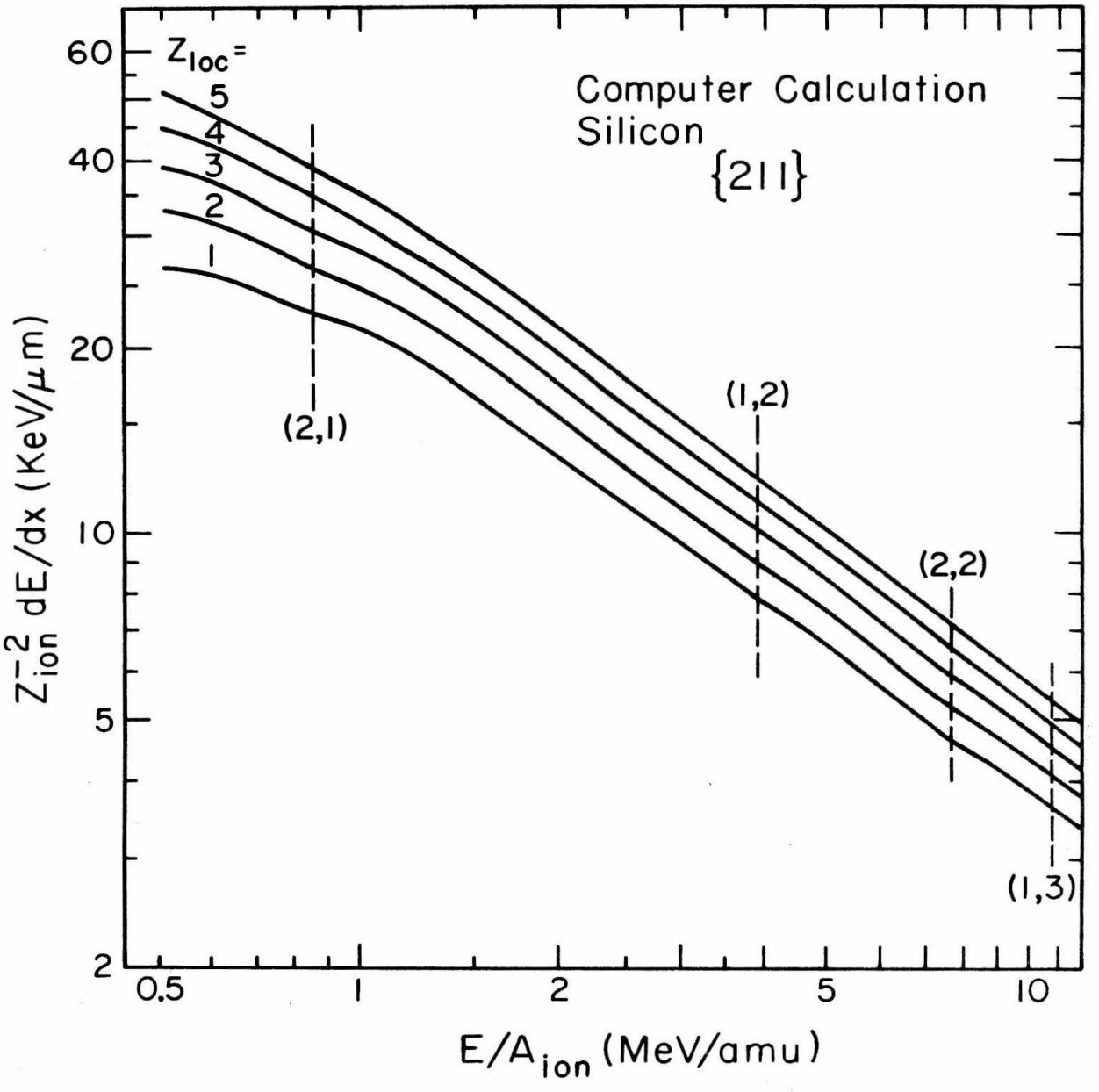
Z_{loc}=
5
4
3
2
1
Computer Calculation
Silicon
{211}
(2,1)
(1,2)
(2,2)
(1,3)
60
40
20
10
5
2
0.5
1
2
5
10
Z_{ion}^{-2} dE/dx (KeV/μm)
E/A_{ion} (MeV/amu)

Figure 1(h)

V. DESCRIPTION OF THE EXPERIMENTAL SYSTEM AND PROCEDURE

A. Physical Layout

The California Institute of Technology 3 MeV Van de Graaff accelerator in Kellogg Laboratory was used. Beams of protons, H_2^+ , H_3^+ , and He^+ were extracted at energies from .5 to 1.6 MeV, analyzed in a 90^o magnet, and transmitted through silicon crystal targets around 1 μm thick. These targets were mounted in a holder which has a .015" diameter hole to admit the beam. The target was positioned so that its point of minimum thickness was in line with the hole. The size of the beam spot allowed to hit the target and holder was a rectangle, .025" wide by .100" high which completely covered the .015" hole.

The beam transmitted through the target either struck a scintillation screen two inches away when the crystal was being aligned (see subsection F), or, when taking a spectrum, passed through the .004" wide entrance slit of an 8-inch radius 162^o, $n = 1/2$ analyzing magnet.

This magnet was the principal tool used to measure the transmission energy spectrum. It was built for the 600 KeV accelerator and, after many years of disuse, was renovated and installed on the 3 MeV accelerator. Its design and the general theory of $n = 1/2$ magnets are discussed by Snyder (1948) and in subsection D below.

The analyzed transmitted beam was passed through a .004" wide magnet exit slit, a multiple scattering foil (6.5μm thick aluminum) 11/16" away to reduce the beam intensity on the detector, another .004" slit two inches from the foil, and then into a surface barrier detector.

The second slit eliminated most multiple scattered particles, thereby reducing the counting rate in the detector to safe levels. It also gave the detector a very narrow angular resolution. It was found from experience that this was necessary to eliminate slit scattered particles which completely distorted the transmission spectra obtained. (Note: The 6.5μm foil was only used for data $\geq$ .8 MeV).

Figure 2 gives the physical layout of the system, the beam path, and all the magnets, slits, and slit settings used.

B. Magnet Field Measurements and Beam Energy Calibration

The 90^{o} and 8-inch magnets are monitored by Siemens model FC34 Hall probes, which have a rated sensitivity of 13 mv/ kG/100 ma control current, and a mean temperature coefficient of $-.06\%/^{o}C$ (Appendix A).

The 90^{o} magnet contains two Hall probes. One of them, which we will refer to as the "old" Hall probe, has been in the magnet with its control current continuously on (except for brief periods) for several years. It was calibrated four times since December 1972 and two of those times showed less than .5% variation from the 1972 calibration voltages. The other two times the calibration gave .77 to 3.02% larger Hall probe readings than the 1972 calibration predicted. In both cases the experimenters did not know if the temperature regulation in the Hall probe assembly was working properly. The Hall probe has a negative temperature coefficient, so that the discrepancies could be due to accidentally shutting off the heater regulator circuit.

Figure 2

Physical layout of the experimental system. The plane of the drawing is the floor of the target room (Room 100, Kellogg). The accelerator is in a large vertical tank in the room upstairs. The beam tube of the accelerator comes down through the ceiling of the target room and the "cross field" magnet, which deflects the beam slightly to the north, into the 90^{o} analyzing magnet at the point marked A.

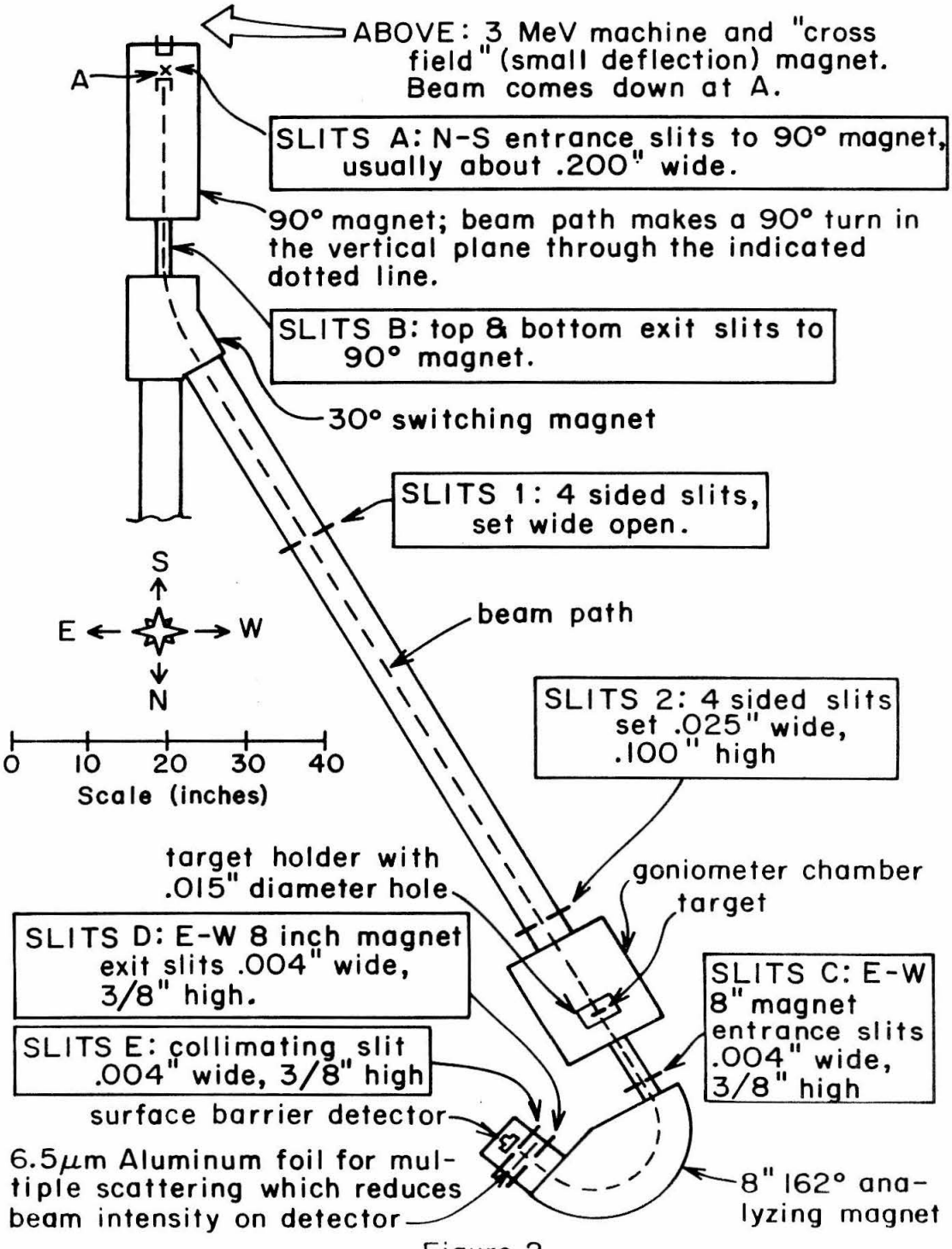
ABOVE: 3 MeV machine and "cross field" (small deflection) magnet. Beam comes down at A.
A
SLITS A: N-S entrance slits to 90° magnet, usually about .200" wide.
90° magnet; beam path makes a 90° turn in the vertical plane through the indicated dotted line.
SLITS B: top & bottom exit slits to 90° magnet.
30° switching magnet
SLITS 1: 4 sided slits, set wide open.
S
E
W
N
0 10 20 30 40
Scale (inches)
beam path
SLITS 2: 4 sided slits set .025" wide, .100" high
target holder with .015" diameter hole
goniometer chamber target
SLITS D: E-W 8 inch magnet exit slits .004" wide, 3/8" high.
SLITS C: E-W 8" magnet entrance slits .004" wide, 3/8" high
SLITS E: collimating slit .004" wide, 3/8" high
surface barrier detector
6.5μm Aluminum foil for multiple scattering which reduces beam intensity on detector
8" 162° analyzing magnet

Figure 2

Throughout the experiment we have used the old Hall Probe and the December 1972 calibration to determine the accelerator energy. Table 2 gives details of the 1972 calibration. The data in the table have been fitted to

$$V_{Hall} = 1.61 \sqrt{x} + .00094x \qquad (29)$$

where

$$x = (\text{mass of the ion/proton mass}) \times E_{ion} \text{ (in MeV)}$$

The second 90^{o} magnet Hall probe and the Hall probe in the 8 inch magnet were installed recently as part of a high precision magnet regulation and sweep system which will be described in the next section. A high-stability control current power supply and Hall probe assembly temperature regulator was built. A description of it with data on its performance is given in Appendix B. According to the analysis of the measured electronic fluctuations given in Appendix B, the Hall probe calibration should remain stable to .06%. During the period when the data reported in this work were taken, the Hall probes remained consistent with each other to .1%. Also, the most recent calibration check done on the 90^{o} magnet old Hall probe differed from the 1972 calibration by less than .1%. Therefore, the error in the data due to energy calibration discrepancies is at least as small as 1 %, and perhaps as small as .2%. (Recall that $E \propto \sqrt{V_{Hall}}$).

The energy loss measurements carried out required calibrating small differences between Hall probe measurements. It was verified

Table 2

December 1972 Calibration of the Old Hall Probe in the 90^{o} Magnet Using Nuclear Resonances

† $F^{19}(p,\alpha\gamma)O^{16}$ resonance at 340.46 ± .04 KeV with width 2.4 ± .2 KeV

* $F^{19}(p,\alpha\gamma)O^{16}$ resonance at 872.11 ± .02 KeV with width 4.7 ± .2 KeV

\+ $A^{27}(p,\gamma)Si^{28}$ resonance at 991.90 ± .04 Kev with width .10 ± .02 .

All energies are in the laboratory frame of reference.

Table 2

Beam		V_{Hall}^{exper}	V_{Hall}^{calc}	$\Delta = V_{Hall}^{exper} - V_{Hall}^{calc}$	$\frac{100\Delta}{V_{Hall}^{exper}}$
M (proton masses)	E (KeV)	experimental (mv)	Calculated with equation (29) (mv)	(mv)	(%)
1.0000	872.11*	48.34 ± .01	48.366	.026	.054
1.0000	991.90+	51.67 ± .01	51.638	-.032	-.062
2.0005	680.92†	60.72 ± .03	60.702	-.018	-.030
3.0011	1021.38†	91.95 ± .05	92.019	.069	.075
2.0005	1744.22*	98.34 ± .04	98.383	.043	.044
2.0005	1983.80+	105.22 ± .01	105.155	-.065	-.062
				sum=.023	

that

$$V_{Hall} = \text{constant} \times \sqrt{ME}$$

held to .07% accuracy for the 8 inch magnet Hall probe measurements. We will assume this is still true for small differences of Hall probe measurement, which is reasonable since otherwise the V_{Hall} (E) curve would have localized irregularities. The net error in dE/dx measurements due to energy calibration uncertainties for the Hall probes is thus less than 1 %, and we may assume that $V_{Hall} \propto \sqrt{ME}$ when analyzing transmission spectra.

C. Magnet Field Regulation and Sweep System

The power supplies of the 90^{o} and 8 inch magnets were regulated by control circuits so that the voltages V_{Hall} of their Hall probes agreed with an adjustable stable reference voltage V_{ref} (plus, optionally, a sweep voltage V_{sweep} in the case of the 8 inch magnet). A Fluke 885AB differential voltmeter was used to provide V_{ref} and to measure the difference between V_{Hall} and V_{ref} $(+ V_{sweep})$. This meter has a long term rated accuracy of .0025%. Its reference voltage can be set at any voltage (effective resolution --1 μvolt) between zero and 1.100000V. Its most sensitive differential voltmeter setting is ±100 μv for full scale meter deflection.

The error voltage $V_{Hall} - V_{ref}(-V_{sweep})$ was amplified by the differential voltmeter and then passed on to the control circuit shown in Figure 3.

Figure 3

Control circuit for feedback regulation of the 90^{o} and 8 inch magnets and for sweeping the field in the 8 inch magnet. One copy of circuit (a) regulates each magnet's power supply so that the voltage of the magnet's Hall probe stays within 10 μvolts of a reference voltage (plus possibly a sweep voltage in the case of the 8 inch magnet). Circuit (b) linearly amplifies the x axis oscilloscope display output of a multichannel analyzer and creates from it (1) a sweep signal for regulating the Hall probe, and (2) a larger sweep signal that is adjusted as close as possible to the magnet power supply's input signal requirement in order to carry out the sweep.

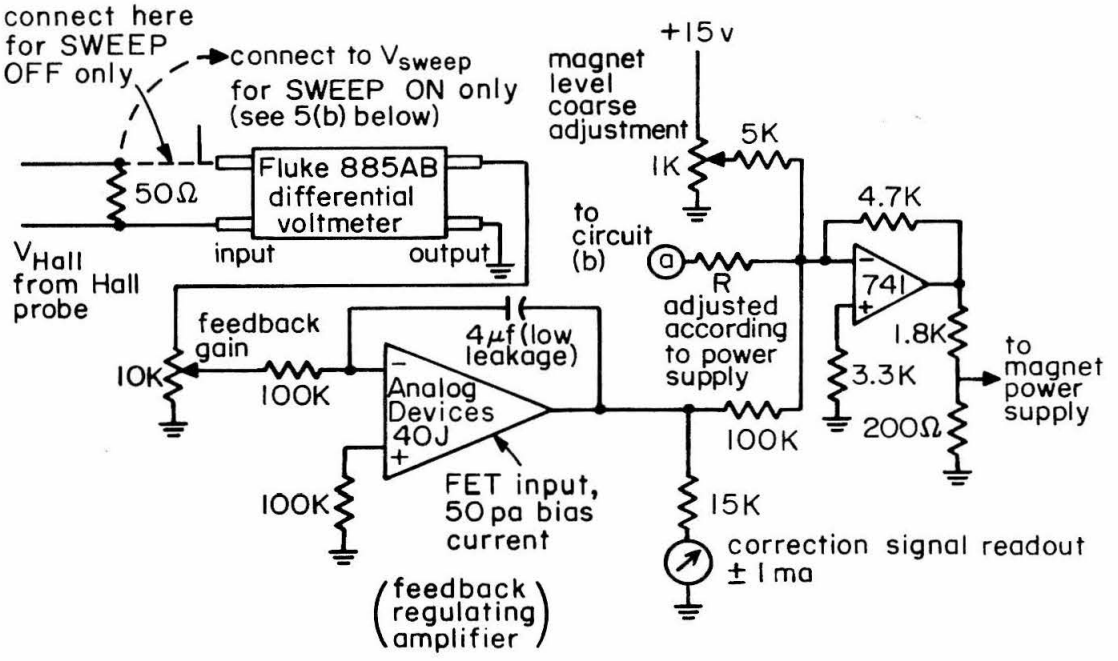

(a) Hall probe feedback regulator

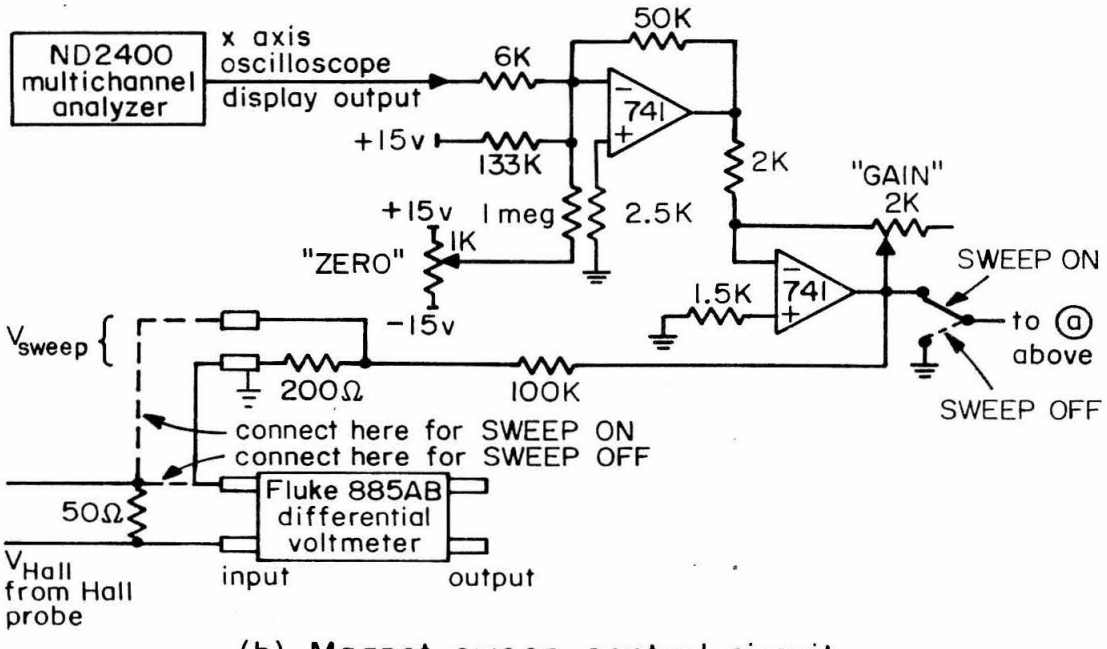

(b) Magnet sweep control circuit

Figure 3

Except for occasional brief transients, this system held the magnets in regulation so that $V_{Hall} = V_{ref}(+V_{sweep})$ always to within ±10 μv, even during 8 inch magnet sweeps as fast as .20 mv/sec. The occasional transients were never successfully tracked down. It is believed that they may be due to pickup in the long lines connecting the control circuits and the magnet power supplies.

A velocity spectrum of the beam transmitted through a target was taken with the following procedure and setup: The beam striking the target holder and target was integrated and digitalized. Every preset number of output pulses from the digitalizer stepped the channel on a Nuclear Data Corporation ND2400 multichannel analyzer used in multiscalar mode. The beam analyzed by the 8 inch magnet was counted by a solid state detector and stored in the currently activated channel of the analyzer. After either 400 or 800 steps the sweep was stopped by an Ortec timer scalar.

The x axis oscilloscope display voltage, which varied linearly with channel number, was amplified, off set, and attenuated by the circuit in Figure 3(b) to create a sweep voltage V_{sweep}. V_{Hall} was regulated as described above and in Figure 3 to increase exactly as V_{sweep} did. Thus, the system assured that the channel number on the stored multichannel analyzer transmission spectrum after an 8 inch magnet sweep would be linearly related to V_{Hall}.

A note about the construction of circuit in Figure 3(b): V_{sweep} was generally of the order of fractions of millivolts. It was

found that if such small voltages were switched on and off through ordinary switches, prohibitively large contact potentials were added to them. Therefore, a system was devised so that V_{sweep} could be added to V_{ref} by unplugging and plugging a patch cord on the front panel. The patch cord was tinned on its plugs at both ends, and the binding posts into which it was plugged were gold plated. No contact potential problems occurred with this new system.

D. Energy Resolution of the Magnetic Analyzers

The 90^{o} and 8 inch magnets are both $n = 1/2$ magnets. This means that the pole faces are slanted so that the magnetic field halfway in between satisfies

$$H(r) = H_{o}\sqrt{\frac{r_{o}}{r}} \tag{30}$$

where r is the radial distance from the center of the magnet, r_{o} is a specific radius, and H_{o} is the magnetic field at r_{o}. Figure 4 gives a detailed diagram of the 8 inch magnet and illustrates the variables r and ϕ to be used in our magnet resolution analysis below.

We follow Snyder (1948) in analyzing the trajectory of a particle through an $n = 1/2$ magnet. Choose as coordinates the radial variable r, azimuthal angle ϕ about the center of the magnet (see Figure 4), and z, the distance away from the midplane of the magnet. We have azimuthal symmetry; therefore the magnetic field has only two components H_{r} and H_{z} and they depend on r and z only.

Figure 4

Diagram of the 8 inch magnet giving details of the target chamber. The variables r and ϕ used in the analysis of the magnet's energy resolution, subsection V D, are illustrated on this diagram.

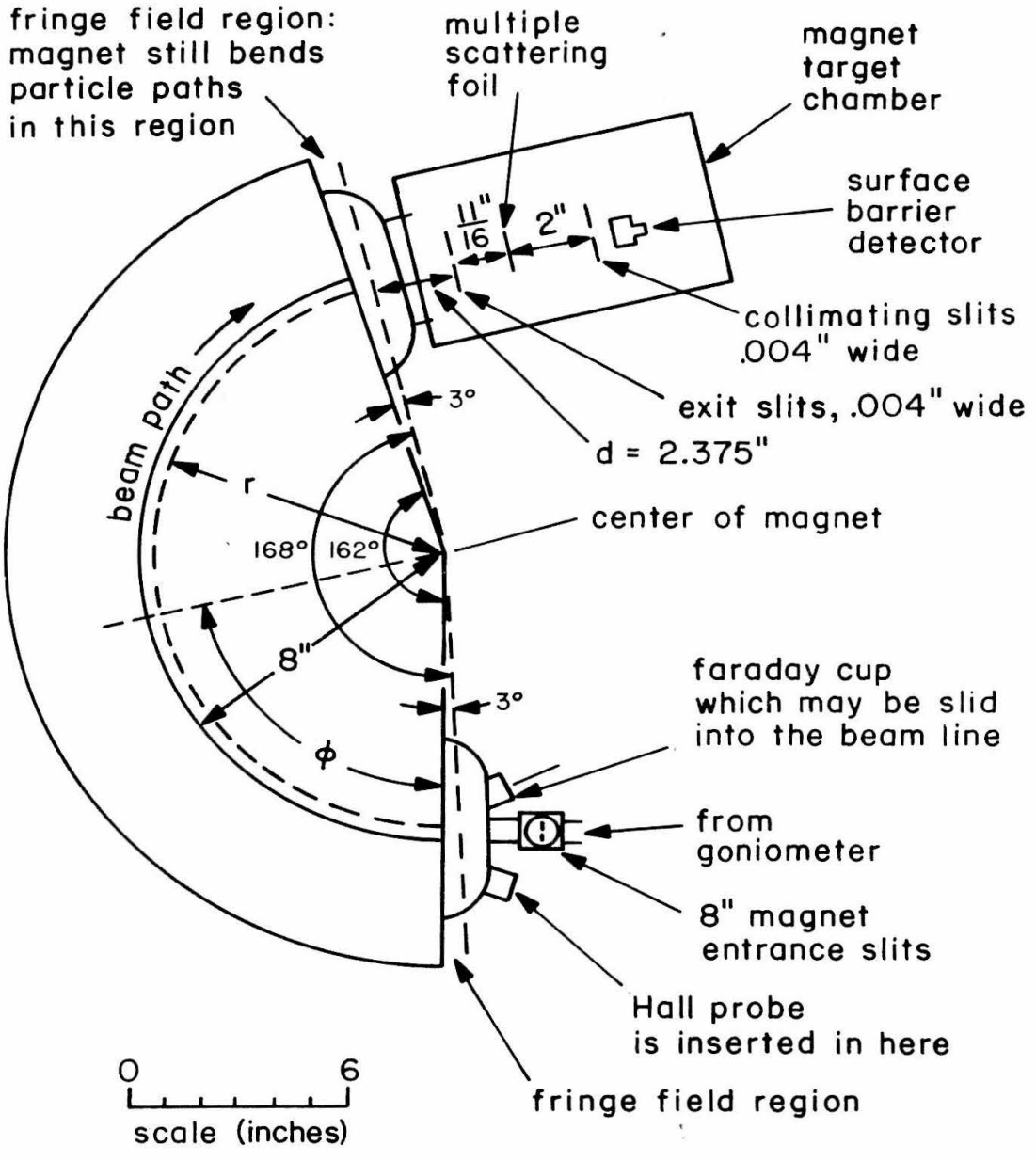
fringe field region: magnet still bends particle paths in this region
multiple scattering foil
magnet target chamber
surface barrier detector
11/16"
2"
collimating slits .004" wide
exit slits, .004" wide
d = 2.375"
3°
beam path
r
center of magnet
168°
162°
8"
3°
φ
faraday cup which may be slid into the beam line
from goniometer
8" magnet entrance slits
Hall probe is inserted in here
fringe field region
0
6
scale (inches)

Figure 4

Furthermore, $H_r = 0$, and H_z satisfies equation (30) when $z = 0$.

The general equations of motion in the magnet for an ion of charge e and mass m are

$$mr\ddot{\phi} = ez\dot{H}_r - er\dot{H}_z - 2mr\dot{r}\dot{\phi}$$

$$m\ddot{z} = -eH_r\, r\dot{\phi}$$

$$m\ddot{r} = eH_z\, r\dot{\phi} + mr\dot{\phi}^2$$

When $z = 0$ and $r = r_o$ = constant we obtain the solution

$$\dot{\phi} = \frac{-H_z e}{m}$$

Define $H_o = H_z(r_o, z = 0)$ and $v_o = r_o\dot{\phi}$. Then we have

$$H_o = \frac{-mv_o}{er_o} \tag{31}$$

Now consider a first order perturbation in this $r = r_o$ orbit. Let z and ρ ($\equiv r - r_o$) be the first order infinitesimal variables. Maxwell's equation states that

$$\frac{\partial H_r}{\partial z} = \frac{\partial H_z}{\partial r}$$

Call this quantity H_o'. Using $\nabla \cdot \underset{\sim}{H} = 0$, we obtain

$$H_r \cong H_o' z$$

$$H_z \cong H_o + H_o'\rho$$

Then, to first order, $mr\ddot{\phi} = -er\dot{H}_o - 2mr\dot{r}\dot{\phi} = -mr\ddot{\phi}$. Thus, $v_o = r\dot{\phi}$ and

$$\ddot{z} + \omega_z^2 z = 0 = \ddot{\rho} + \omega_r^2\rho$$

where

$$\omega_z^2 = \frac{ev_o}{m} H_o'$$

$$\omega_r^2 = -\frac{ev_o}{m}\left(\frac{1}{r_o} H_o + H_o'\right)$$

A beam of particles which diverges from a point in the magnet will be refocused both in the r and z planes if $\omega_r^2 = \omega_z^2$. Let us see what this condition implies:

$$\omega_z^2 - \omega_r^2 = \frac{ev_o}{m}\left(2H_o' + \frac{H_o}{r_o}\right)$$

which is zero if

$$H_o' \equiv \left.\frac{\partial H_z}{\partial r}\right|_{r_o} = \frac{-H_o}{2r_o} \tag{32}$$

or

$$H(r) = H_o\sqrt{\frac{r_o}{r}}$$

precisely the $n = 1/2$ magnet condition. This is the reason why $n = 1/2$ magnets are used.

Thus, to first order, a beam focused at one point will be refocused at another by the $n = 1/2$ magnet. The aximuthal angle between these focal points is, applying equations (31) and (32),

$$\dot{\phi}\frac{\pi}{\omega_z} = \sqrt{2}\,\pi \tag{33}$$

Consider a parallel beam entering the initial magnet slit. Let R be the radius of the trajectory of a particle which passes through the center of both the initial and final slits. (We assume that the

slits are so positioned that there is such a trajectory.) Call this trajectory the standard trajectory. (Refer to Figure 5 for this discussion.)

A particular beam particle entering the initial slit at distance x from the slit center with energy E_o follows the trajectory (to first order in x/R)

$$r = r_o + (x + R - r_o) \cos \frac{\phi}{\sqrt{2}} \tag{34}$$

where ϕ is chosen to be zero at the entrance to the bending region of the magnet, and

$$r_o = \frac{\sqrt{2mE_o}}{-eH_o} \tag{35}$$

(We have used equations (31) and (33).) Let θ be the total angle of bending for the magnet. The particle will leave the magnet at a radial distance

$$r_f = r_o + (x + R - r_o) \cos \frac{\theta}{\sqrt{2}} \tag{36}$$

Define d to be the distance from the end of the bending region of the magnet to the magnet's final slit. Over this distance d the particle will move in a straight line towards or away from the standard trajectory. At the final slit the distance y from the beam to the final slit's center will be given by

$$\frac{y - (r_f - R)}{d} = \frac{\frac{d}{d\theta} r(\theta)}{r_f}$$

Figure 5

Diagram for the discussion of resolution of the 8 inch magnetic spectrometer

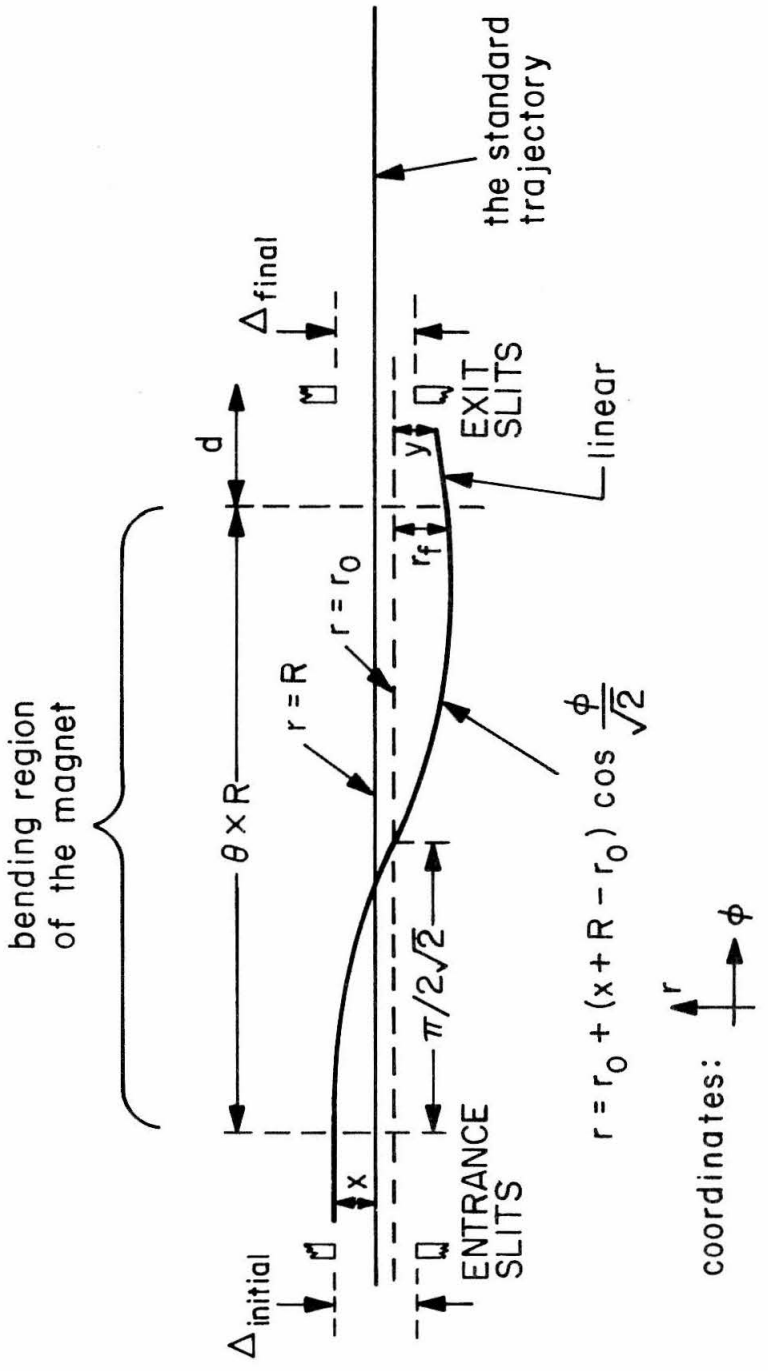
bending region
of the magnet
θ × R
d
Δ initial
Δ final
x
y
r = R
r = r0
rf
π/2√2
ENTRANCE
SLITS
EXIT
SLITS
linear
the standard
trajectory
r = r0 + (x + R − r0) cos φ/√2
coordinates:
r
φ

Figure 5

Substitute equations (34) and (36) into this equation:

$$y + R - r_o - (x + R - r_o) \cos \frac{\theta}{\sqrt{2}}$$

$$= - \frac{d}{\sqrt{2}\ r_f} (x + R - r_o) \sin \frac{\theta}{\sqrt{2}}$$

Assume that the slit widths are small. Then $r_f \cong R$, and we may rewrite this equation to first order as

$$y + R - r_o = -M(x + R - r_o) \tag{37}$$

where

$$M = -\cos \frac{\theta}{\sqrt{2}} + \frac{d}{R\sqrt{2}} \sin \frac{\theta}{\sqrt{2}} \tag{38}$$

This equation shows that M gives the magnification that a beam spot undergoes when the beam passes through the magnet.

To calculate the magnet's energy resolution, we determine the particle trajectories which pass through both magnet slits and have minimum and maximum r_o . Then from equations (30) and (35) we can compute the energies of the particles having these trajectories.

Solve (37) for r_o :

$$r_o = \frac{Mx + y + (1+M)R}{1 + M}$$

Then

$$\Delta r_o \equiv r_{o,max} - r_{o,min}$$

$$= \frac{M(x_{max} - x_{min}) + (y_{max} - y_{min})}{1 + M}$$

$$= \frac{M\,\Delta_{initial} + \Delta_{final}}{1 + M} \qquad (39)$$

where Δ stands for the slit width. Equations (30) and (35) yield

$$H_o = H_R \sqrt{\frac{R}{r_o}} = \frac{\sqrt{2mE_o}}{-er_o}$$

where $H_R = H_z(r = R,\ z = 0)$. Thus

$$E_o = (r_o H_R^2\, e^2 R) / (2m)$$

$$\Delta E_o/E_o = \Delta r_o/r_o$$

When $\Delta_{initial} = \Delta_{final} \equiv \Delta r$, equation (39) gives

$$\Delta E_o/E_o = \Delta r_o/r_o = \Delta r/R$$

For the 8 inch magnet $\Delta_{initial} = \Delta_{final} = \Delta r = .004"$, $R = 8"$, $d = 2.375"$, $\theta = 168^o$. Therefore

$$M = 0.666$$

$$\text{Energy resolution} = \Delta E/E = .05\%$$

The energy resolution of the 90^o magnet was not analyzed. Instead the accelerator and 90^o magnet were evaluated experimentally using the

8 inch magnet to see what energy spectrum the beam had. By adjusting slits A and B (see Figure 2), an approximately trapezoidal energy distribution of width 1 to 3 Kev was always obtained.

E. Target Preparation

The targets used were aligned single silicon crystals around 1 μm thick obtained from Dr. Frederick Eisen at Rockwell International Science Center, Thousand Oaks, California.

These targets were prepared by Dr. Eisen as follows. Thin silicon slices were lacquered on the edges (to prevent etching of the edges) and etched in 6 parts nitric acid, 3 parts acetic acid and 1 part HF acid until they became transparent. These targets were then attached to small aluminum mounts by placing them on wax over a hole in the mount and heating just enough for the wax to melt. When the heat was removed the wax stretched and bonded the target over the hole. Next this small aluminum mount with the target on it was placed under sodium light and the point of minimum thickness of the target was found by observing Newton's rings. The mount was then clamped between two circular pieces, one of which had a .015" diameter hole, the other a larger hole, so that the .015" hole was centered over the point of minimum thickness of the target. The assembly, which we shall refer to as the target holder, is shown in Figure 6.

The small mount was positioned by means of set screws so that the target was as near to the .015" hole as possible. This hole had slanted edges allowing beam incident on the target holder at various

Figure 6

Diagram of the target holder assembly

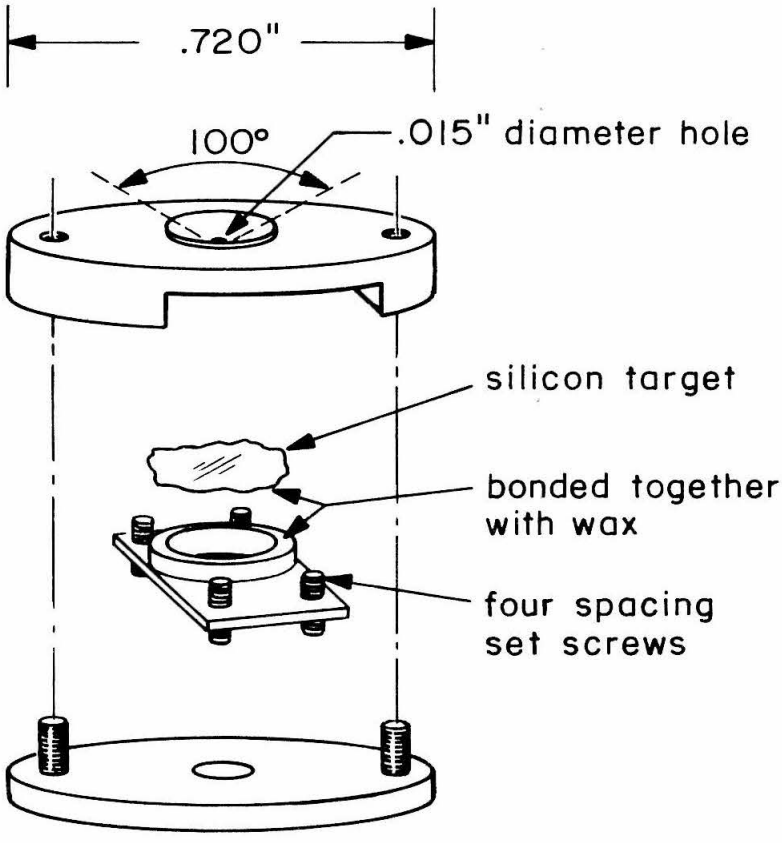
.720"
100°
.015" diameter hole
silicon target
bonded together
with wax
four spacing
set screws

Figure 6

angles to pass through the same .015" diameter part of the target.

The target thicknesses were around 1 μm, measured by Eisen using a Cary 14 spectrophotometer. His method was successfully duplicated at Caltech. The target, mounted in its holder, was placed in the spectrophotometer and optical absorption over a range of wavelengths (for instance, 9000Å to 12000Å) was measured and plotted. The absorption curve oscillated almost sinusoidally. Target thickness is computed from the value or difference in values of the wavelengths at successive peaks or valleys on this curve as follows: Consider a two-boundary reflection-transmission problem. Wave $e^{i(kx-\omega t)}$ enters from the left in a region having unity index of refraction n. At $x = 0$ it enters a region with nonunity $n = n$, and at $x = \Delta x$ it leaves this region and enters a second $n = 1$ region. If T is the amplitude for transmission and R that for reflection, we can write down representations for the wave in each region. The equations for the wave and its first derivative to be continuous at the region boundaries $x = 0$ and $x = \Delta x$ yield

$$|T|^2 = 1 - |R|^2$$

$$R = \frac{i(n^2 - 1)\sin(nk\Delta x)}{2n\cos(nk\Delta x) - i(1+n^2)\sin(nk\Delta x)}$$

The $\sin(nk\Delta x)$ determines the maxima and minima in $|R|^2$ to within .05% as was verified by a detailed calculation. To this accuracy, therefore, if λ_1 and λ_2 are two successive maxima or two successive minima we have the equation

$$\Delta x = \text{target thickness} = \frac{\pi}{n(k_2)k_2 - n(k_1)k_1}$$

or, in terms of λ

$$\Delta x = \frac{1}{2} \quad \frac{1}{n(\lambda_2)/\lambda_2 - n(\lambda_1)/\lambda_1}$$

Alternatively, if the order N of the peak or valley is known, then

$$\Delta x = \begin{cases} \frac{1}{2} & \frac{N + \frac{1}{2}}{n(\lambda)/\lambda} \quad \text{for maxima} \\ \frac{1}{2} & \frac{N}{n(\lambda)/\lambda} \quad \text{for minima} \end{cases}$$

$n(\lambda)$ has been measured by Briggs (1950). A graph of the values in his table of results appears in Figure 7.

F. Target Alignment

Before taking a transmission spectrum the target must be aligned for channeling along a particular axis or plane, or for random (nonchanneling) transmission. We begin with a description of the standard alignment technique used at Caltech for backscattering channeling experiments. The target is rotated about two axes over a small range of angles away from orientation perpendicular to the beam. Back scattering is monitored with a detector positioned 150^{o} from the incident beam direction. The detector output is amplified and fed into a single channel analyzer set at a window just below the leading edge of the backscattering spectrum, and then into a count rate meter.

Figure 7

Graph of the index of refraction $n(\lambda)$. Data are from the table in Briggs (1950).

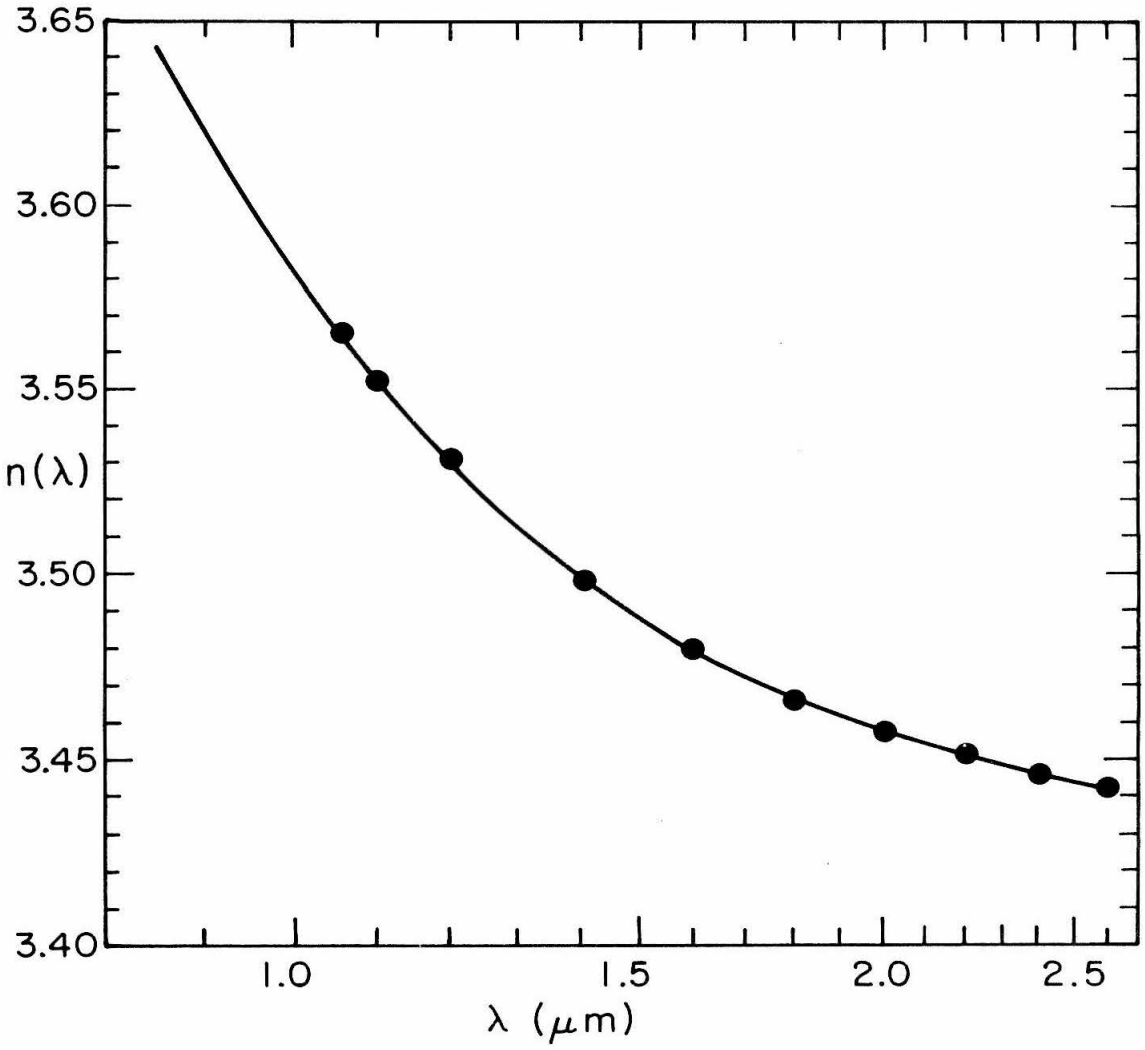

Figure 7

Whenever channeling occurs, incident particles penetrate much deeper into the target before backscattering. Therefore the count rate in the window described drops drastically. In a good crystal the drop will be over 95%. By plotting the angular positions at which back scattering dips occur and interpolating, a drawing such as that in Figure 8 is obtained. The axial channel is at the intersection of the lines correspoinding to planar channels.

Figure 8 is a part of the silicon blocking diagram, the spherical map of all angles of rotation at which axes or planes of the target crystal are aligned with the beam.

Crystaline silicon has a diamond structure (see Figure 9). A flat plane projection of its complete blocking diagram with labeled planes and axes appears in Figure 10. Planes and axes in a drawing such as Figure 8 are identified by comparison with the blocking diagram. Both the geometrical layout and the relative "intensity" (amount of reduction of backscattering) must be matched. Relative intensities can be estimated from the plausible assumption that the larger the interaxial or interplanar space, the more the beam is transmitted, and therefore the greater the reduction or backscattering. The results of such estimates are shown pictorially in Figure 10 through relative line thicknesses, and the sizes of various planar and axial channel spaces for silicon have been given in Table 1.

The backscattering technique proved difficult to use because unsteadiness in the accelerator beam intensity caused stray dips in the backscattering count rate. Instead of monitoring backscattering,

Figure 8

Example of a crystal alignment diagram obtained by monitoring the backscattered or transmitted beam intensity. The points are at the observed angles of backscattering reduction or transmission intensification. Lines drawn between them in practice do not intersect in one point (as shown). This is entirely due to measurement inaccuracy.

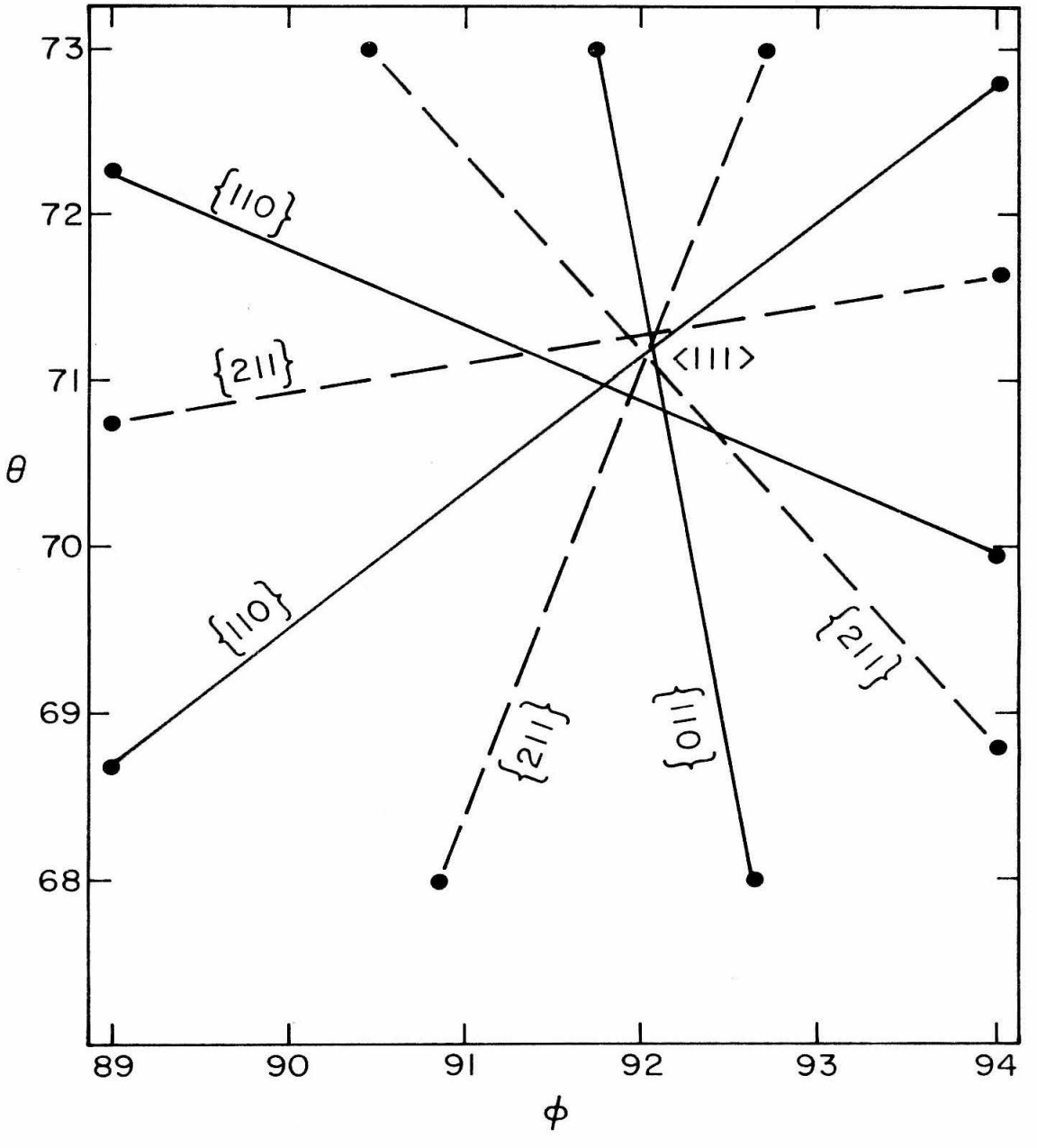

Figure 8

Figure 9

A standard cell for silicon's crystal structure
(diamond type face centered cubic)

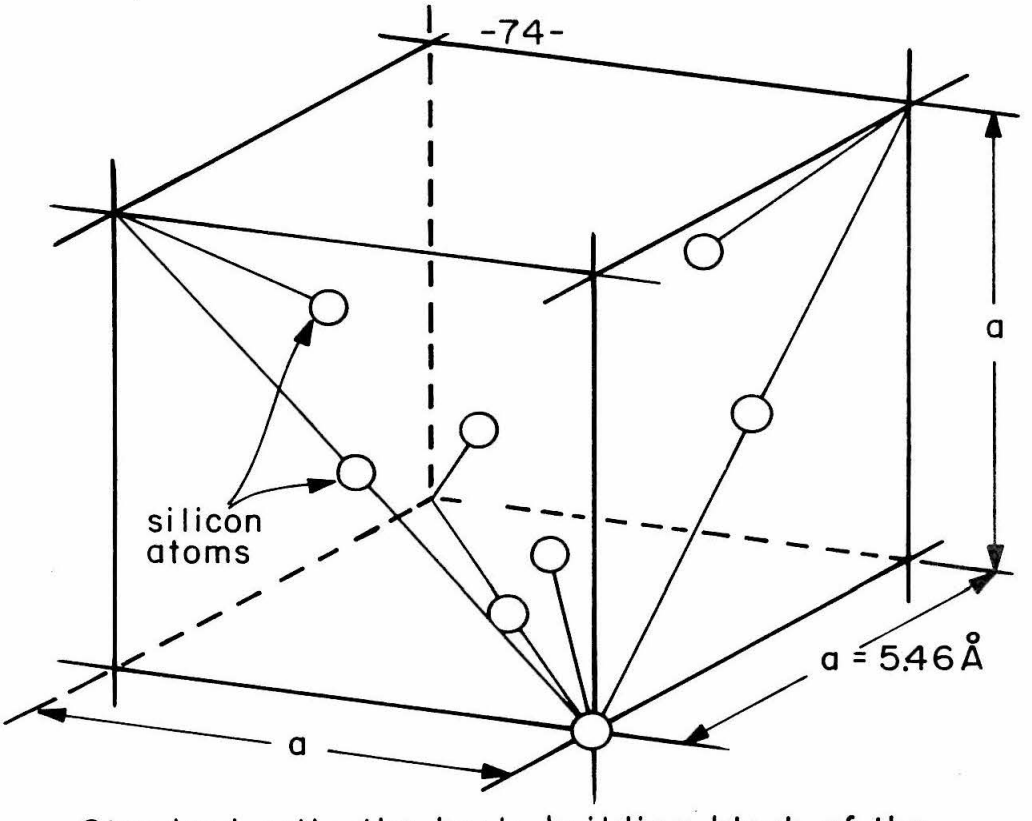

Standard cell – the basic building block of the lattice.

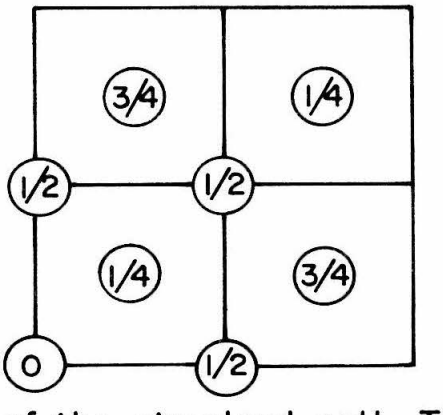

Side view of the standard cell. The numbers indicate distance (in units of a = 5.46 Å) into the paper to the atoms.

Figure 9

Figure 10

Plane projection of a portion of the blocking diagram for silicon. Line widths increase with relative planar channel widths.

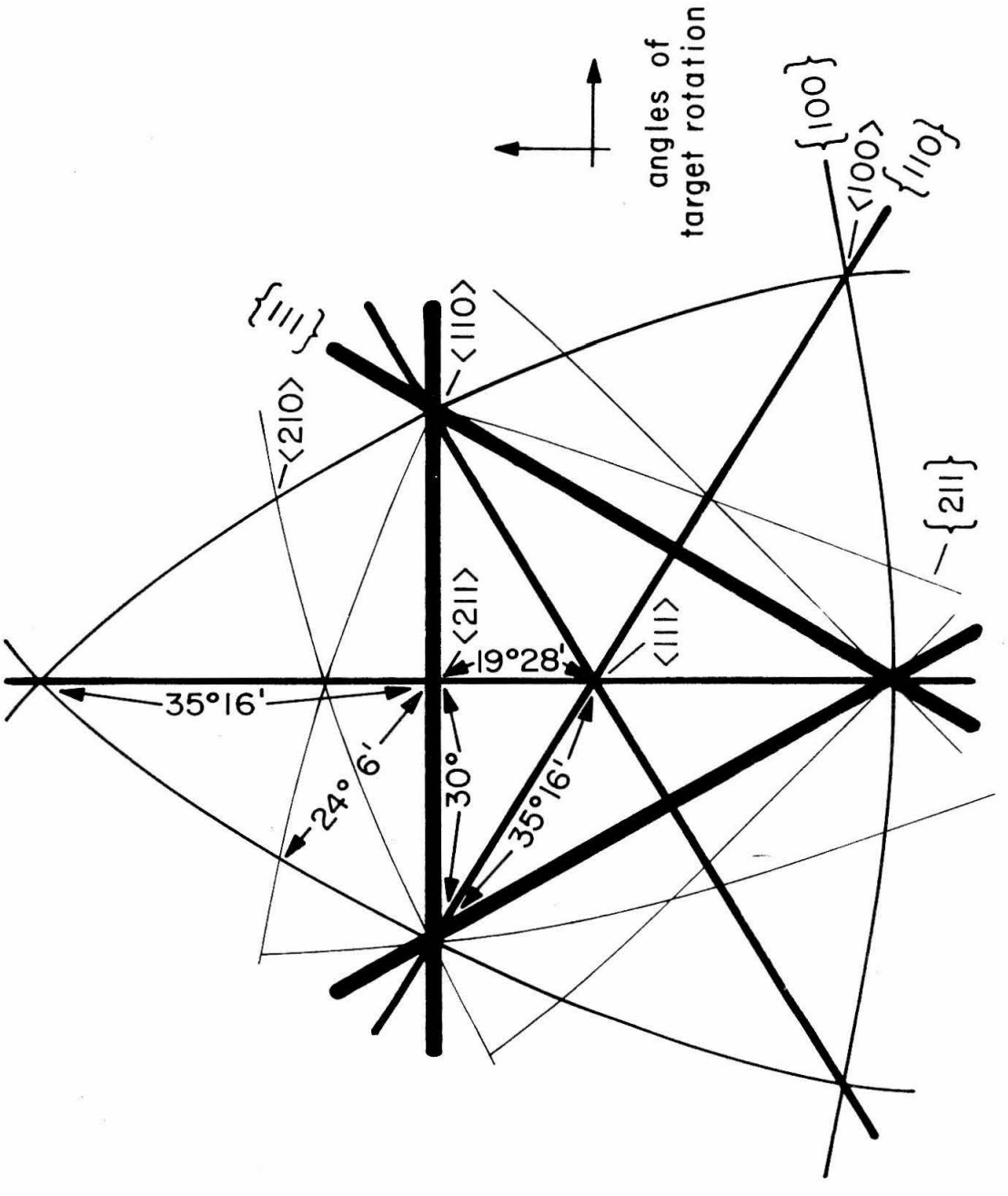
angles of
target rotation
{100}
<100>
{110}
{111}
<110>
<210>
{211}
<211>
<111>
19°28'
35°16'
24° 6'
30°
35°16'

Figure 10

transmission through the target and the 8 inch magnet was tried with much greater success. The magnet was set for an energy above that of randomly transmitted particles and in the range of that for channeled particles coming out of the target. Thus, transmitted beam was only observed at channeling orientations.

In order to eliminate the effects of beam fluctuation the magnet sweep system described in Section C was used to take spectra, except that instead of the magnetic field being stepped, the angular orientation of the target was stepped. Thus the spectra gave beam through the magnet versus angular orientation. These spectra were quite clear. They showed zero counts until a planar or axial channel was crossed. Then a peak of height depending on the channel was obtained. From these data drawings such as Figure 8 were drawn once again.

All of the above techniques for aligning the target were tedious and involved lengthy exposure of the target to the beam, which furthered crystal damage. Another technique (used by F. Eisen and coworkers) was tried with great success. A scintillating screen was installed in the target chamber so that it could be slid behind the target and observed visually. When approximately one nanoamp of beam passed through the target one saw a clear transmission blocking diagram with a bright central spot (the 0^{o} part of the transmitted beam). Whenever channeling occurred the whole pattern diminished to a single brilliant point. By this technique targets were quickly aligned and axes and planes quickly identified.

It was found that axial channeling is sensitive to as little as $\pm.02^{o}$ change in target orientation. By observing the channeling, we demonstrated that the goniometer could be set and reset repeatedly to a given orientation with at least this accuracy simply by reading the angular dials. Therefore we will take $\pm.02^{o}$ as the estimated error for the target orientation in the experiments.

This small figure applies, however, only after successful alignment of the target for channeling. Inaccuracy in alignment proved to be the primary source of experimental error. Of the methods described, the scintillator was most effective (better even than maximizing transmission in some energy window) for finding the channeling orientation that gave the smallest energy loss. But even the scintillator alignments had an unpleasant element of luck. On the final data runs reported in this work complete transmission spectra were taken at four to six $.05^{o}$ steps across a planar channel in order to obtain optimum planar channeling spectra. This proved to be the only reliable way to get best channeled energy loss data.

G. Beam Divergence

The trajectory of particles in the beam was studied by bringing a beam through a .015" diameter hole in a target holder simulator and through the 8 inch magnet (which has .004" wide slits) with slits 1 and 2 opened up (see Figure 3 for slit nomenclature). Then slits 1 and 2 settings were reduced as much as possible without reducing the beam through the magnet.

We would expect the beam that passed into the magnet to have cross section corresponding to the intersection of a tall .004" wide

slit and a circular .015" diameter hole. This is roughly a .004" by .015" rectangle. For the data in Table 3 the following beam cross sections at slits 1 and 2 were obtained by the technique described in the paragraph above:

Calculated Beam Energy (Kev)	Slits 1 Beam Cross Section	Slits 2 Beam Cross Section
935.77	.006" x .019"	.007" x .012"
970.56	.008" x .024"	.007" x .013"
1005.97	.015" x .023"	.007" x .019"

Error bars are approximately ±.002" for these data. The angular divergence appears to be small. The largest decrease in beam dimension from slits 1 to slits 2 is .024" to .013", a decrease of .011". The distance between slits 1 and 2 is 60". Thus we have

$$\text{Full angle of beam divergence} \leq .011"/60" \text{ radians}$$
$$= .00018 \text{ rad} = .011^{o}$$

A note concerning beam trajectory: When the above beam cross sections were measured, it was also found that the center of these cross sectional areas shifted slightly (around .005") from one energy setting of the accelerator to another. If the east-west position of the goniometer was not adjusted for maximum beam transmission into the 8 inch magnet after each energy change, the transmission spectra obtained would occasionally be wrong. (The deceptive data probably came from particles that had undergone small angle scattering before and/or after passing through the target.

VI. EXPERIMENTAL DATA; COMPARISON WITH OTHER DATA IN THE LITERATURE AND WITH THE COMPUTER CALCULATIONS

A. Description of the Data

Data were taken on two targets. One had a <111> axis perpendicular to its surface, and thickness as measured by the Cary 14 technique described in subsection VE of 1.179 μm ±.7% . The other had a <110> axis perpendicular to its surface and Cary 14 measured thickness of 1.217 μm ±.3%.

Figure 11 gives all of the data obtained, along with data reported by other researchers in the literature.

1. Data Taking Procedure

The following procedure was used for obtaining and reducing the data: The beam was transmitted through the target into the 8 inch magnet after target alignment was completed. The magnet was swept over a range sufficiently large to analyze particles with energies below the minimum energy of the transmission spectrum to above the incident beam energy. The spectrum was recorded on the multichannel analyzer. In the middle of the sweep, when the magnet was analyzing particles of energy between those of all particles transmitted through the target and those in the incident beam, the sweep was stopped momentarily and the target was rotated 90^{o}. This allowed some of the incident beam to pass below the target and to be recorded in the same spectrum as the sweep was finished.

The resulting spectra were plotted and the V_{Hall} for the 8 inch magnet for the first and last channels was recorded. An example is shown in Figure 12. By linear interpolation, V_{Hall} values corresponding to (1) the incident beam, (2) the peak of the transmission spectrum, and (3) the extrapolated leading edge of the transmission spectrum (see subsection IIIC) were calculated. The peak and extrapolated leading edge energy losses were then computed by assuming

$$V_{Hall} = \text{constant} \times \sqrt{ME}$$

The equation used was

$$E_{loss} = \left[1 - \left(\frac{V_{Hall}^{spectrum}}{V_{Hall}^{beam}}\right)^2\right] \times (\text{nominal accelerator beam energy})$$

Finally, dE/dx was obtained by division of E_{loss} by the target thickness obtained using the Cary 14.

2. Specifics Concerning the Data Taken

The first accelerator runs with the <111> target gave data with very little scatter, for most points less than 1% scatter. The averages of these data are depicted in the plots in Figure 11 by the open symbols. A final run was carried out with the <111> target two weeks later, after which carbon was discovered on the .015" diameter section of the target used. These data are included in Figure 11 (a

Figure 11

Rate of energy loss data in this work and in the published literature for light ions channeling in silicon. See the text, subsections VIA2 and 4, for details and explanations about the plots and for the meanings of P, PG, and LE.

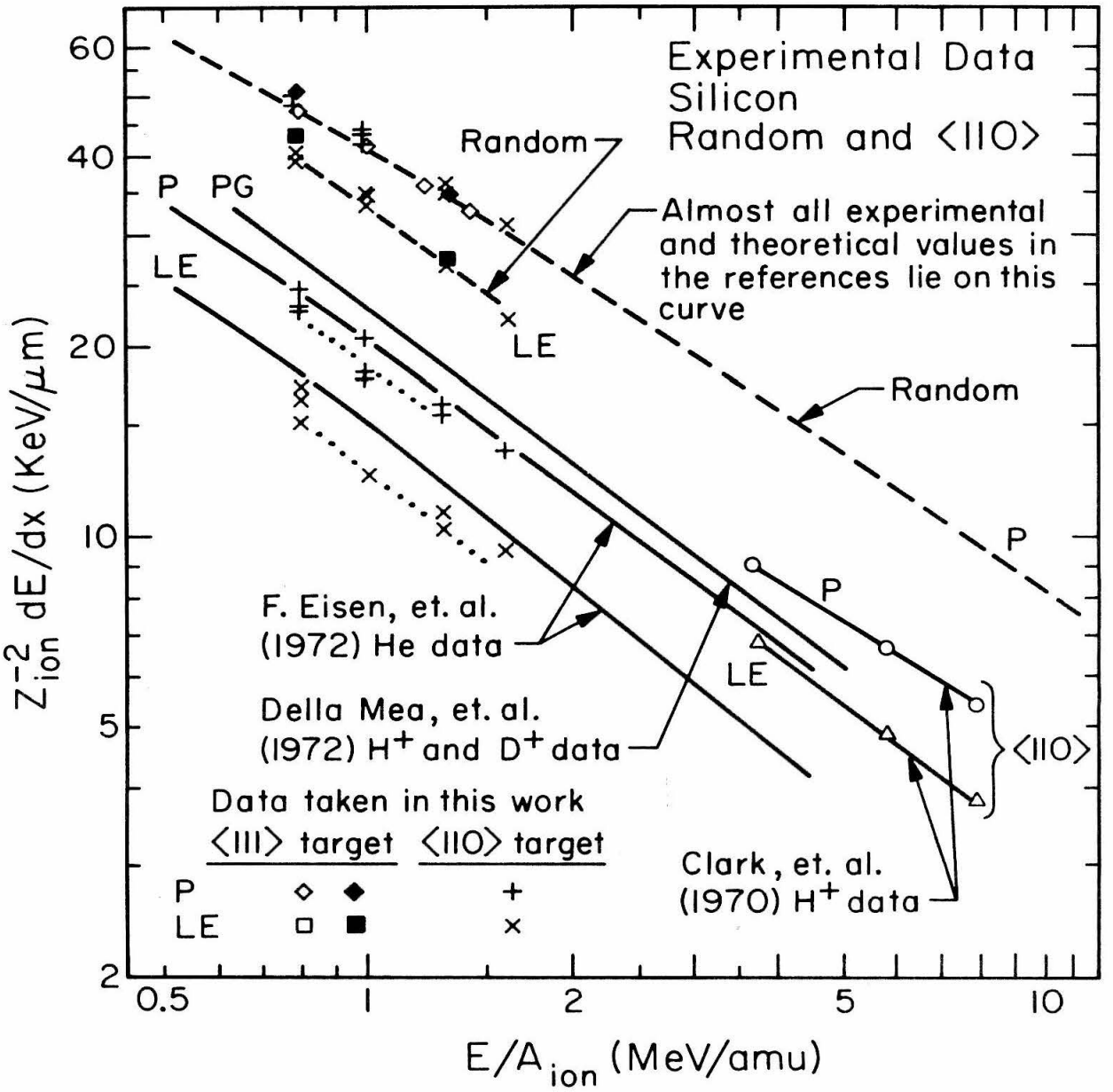
Experimental Data
Silicon
Random and <110>
Random
Almost all experimental and theoretical values in the references lie on this curve
Random
P
PG
LE
LE
P
P
LE
F. Eisen, et. al.
(1972) He data
Della Mea, et. al.
(1972) H+ and D+ data
<110>
Data taken in this work
<111> target
<110> target
P
LE
Clark, et. al.
(1970) H+ data
60
40
20
10
5
2
0.5
1
2
5
10
Z-2ion dE/dx (KeV/μm)
E/Aion (MeV/amu)

Figure 11(a)

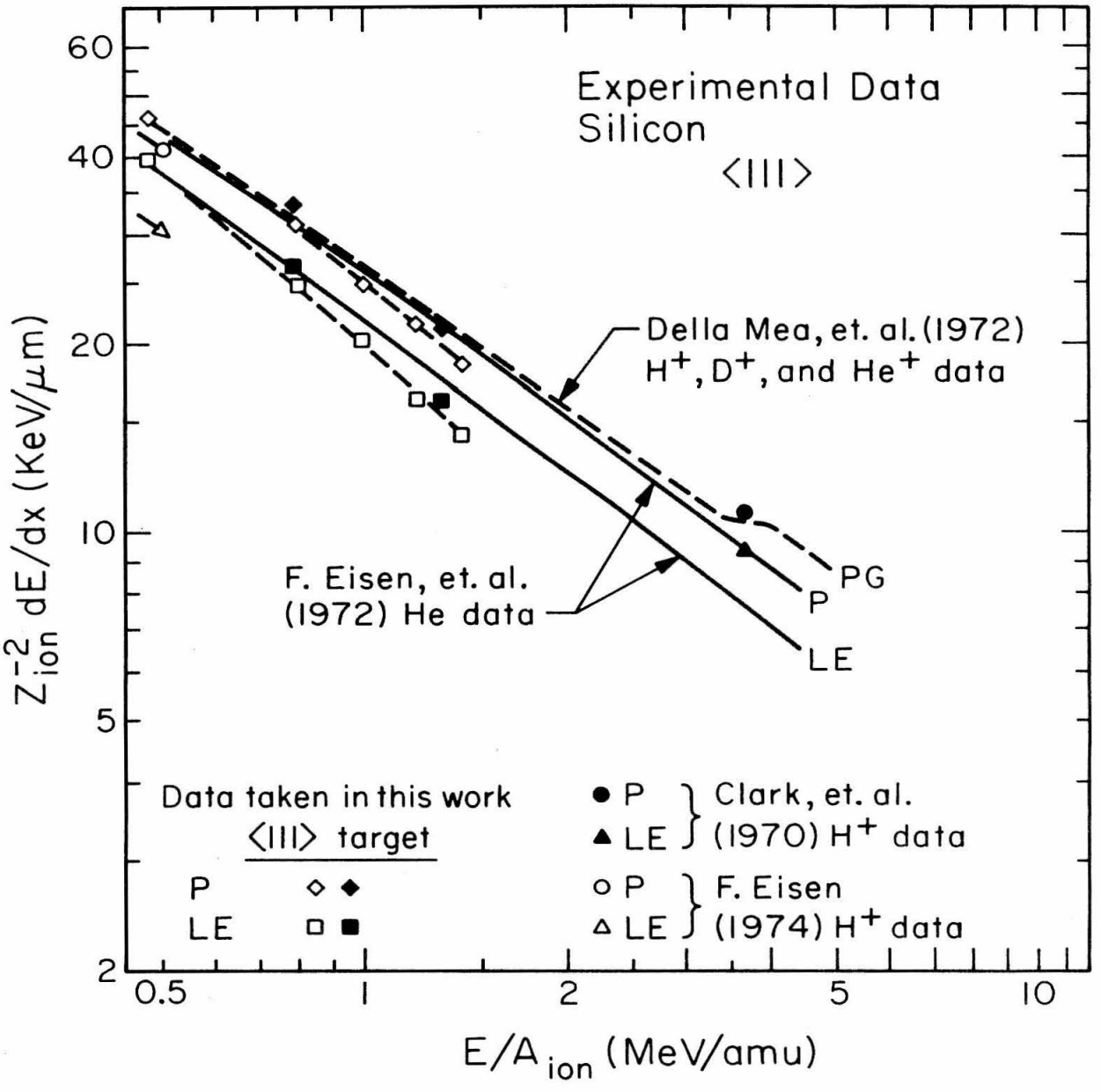
Experimental Data
Silicon
⟨111⟩
Della Mea, et. al. (1972)
H+, D+, and He+ data
F. Eisen, et. al.
(1972) He data
PG
P
LE
Data taken in this work
⟨111⟩ target
P
LE
P
LE
Clark, et. al.
(1970) H+ data
F. Eisen
(1974) H+ data
60
40
20
10
5
2
0.5
1
2
5
10
Z_{ion}^{-2} dE/dx (KeV/μm)
E/A_{ion} (MeV/amu)

Figure 11(b)

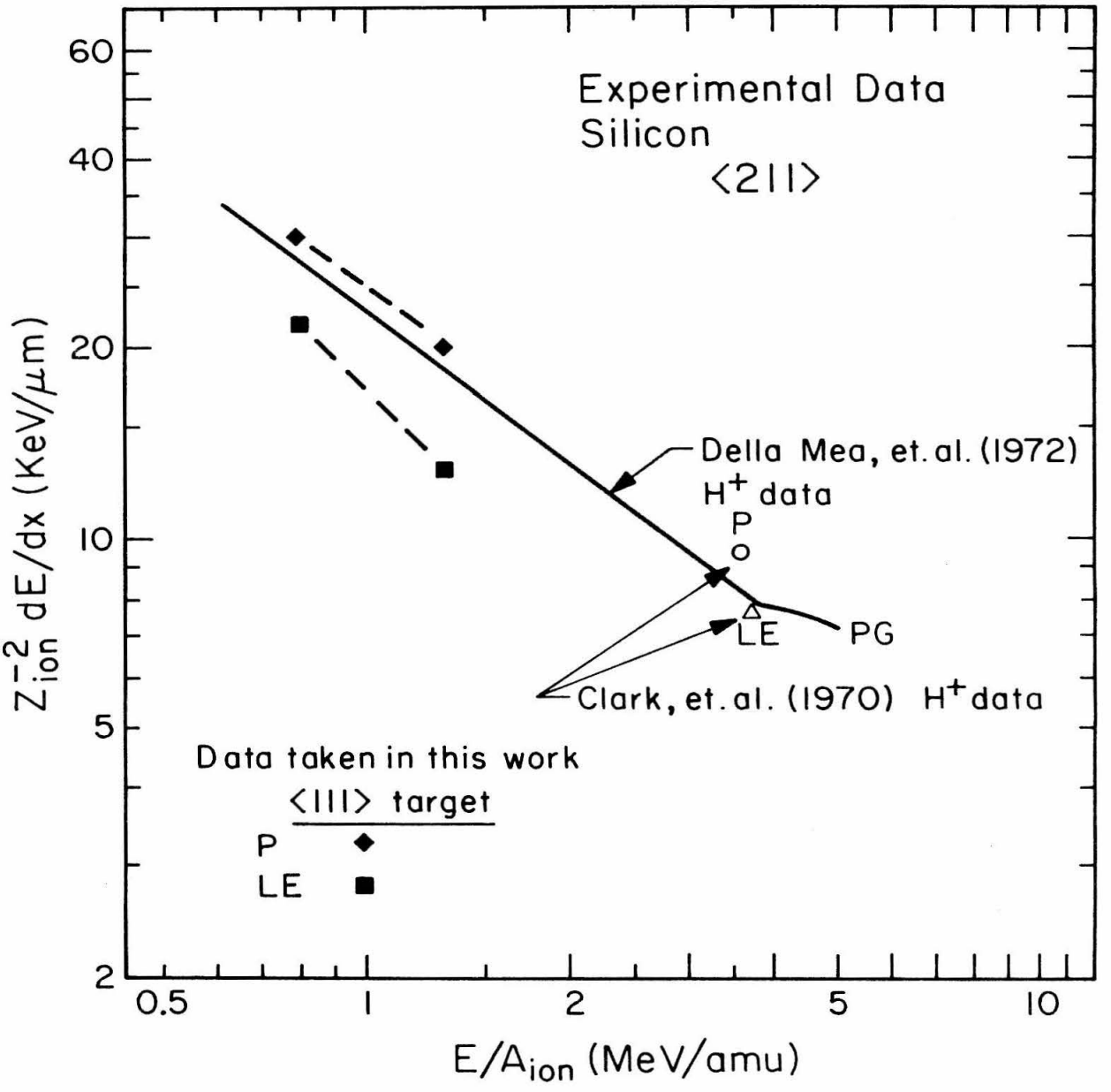
Experimental Data
Silicon
<211>
Della Mea, et.al. (1972)
H+ data
P
O
LE
PG
Clark, et.al. (1970) H+ data
Data taken in this work
<111> target
P
LE
60
40
20
10
5
2
0.5
1
2
5
10
Z-2ion dE/dx (KeV/μm)
E/Aion (MeV/amu)

Figure 11(c)

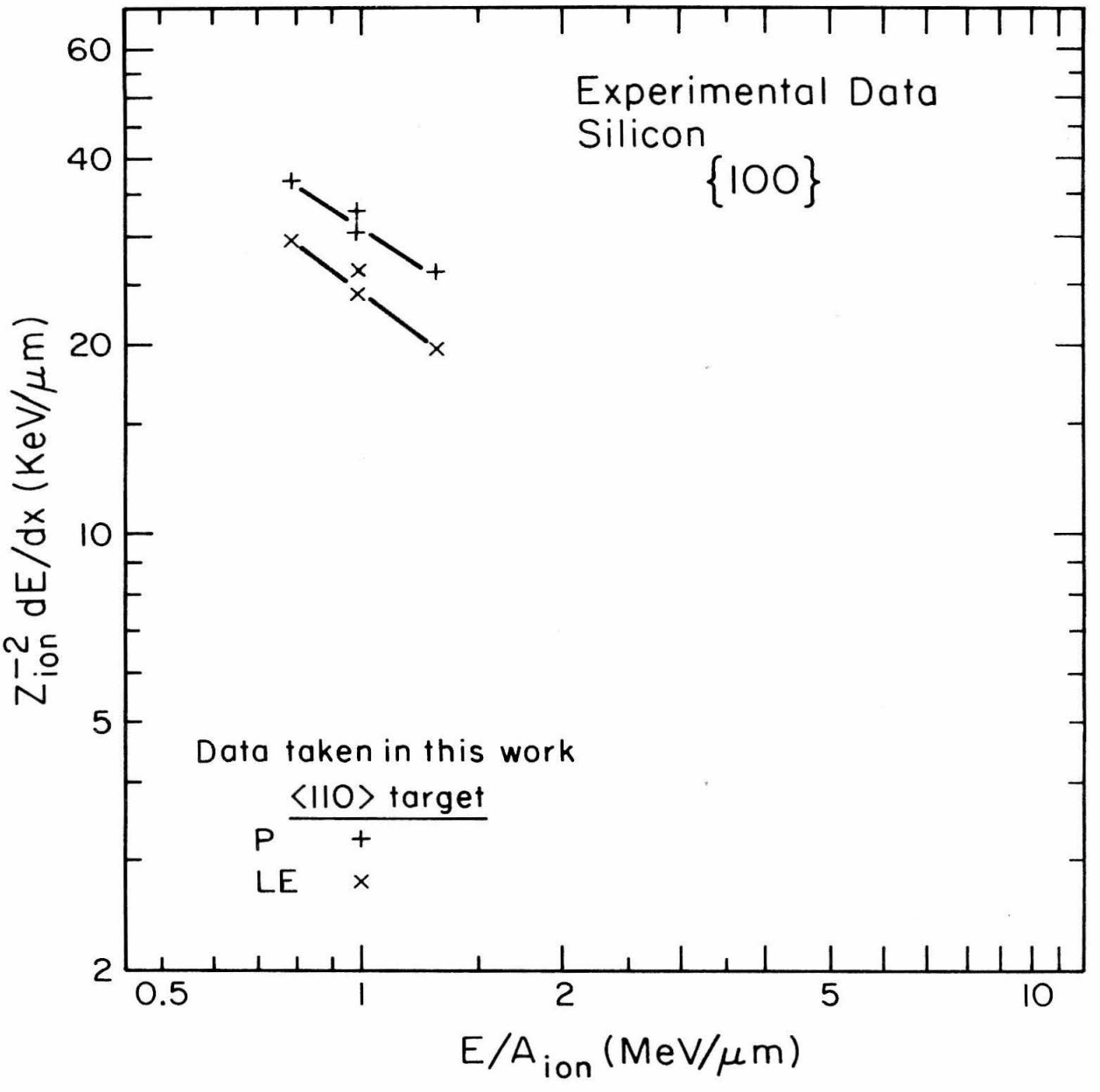
Experimental Data
Silicon
{100}
Data taken in this work
<110> target
P +
LE ×
60
40
20
10
5
2
0.5
1
2
5
10
Z_{ion}^{-2} dE/dx (KeV/μm)
E/A_{ion} (MeV/μm)

Figure 11(d)

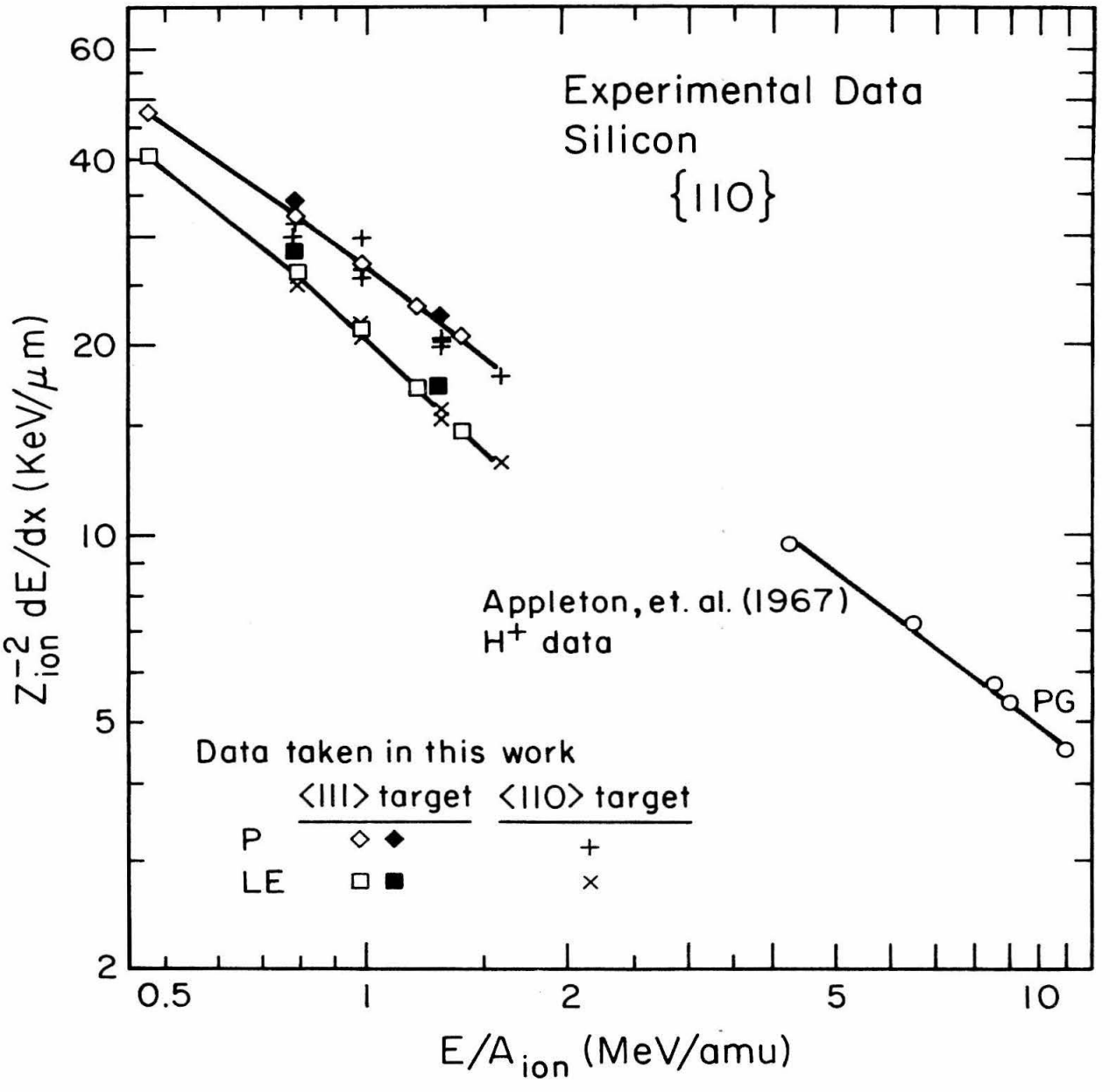
Experimental Data
Silicon
{110}
Appleton, et. al. (1967)
H+ data
PG
Data taken in this work
<111> target
<110> target
P
LE
60
40
20
10
5
2
0.5
1
2
5
10
Z-2 ion dE/dx (KeV/μm)
E/A ion (MeV/amu)

Figure 11(e)

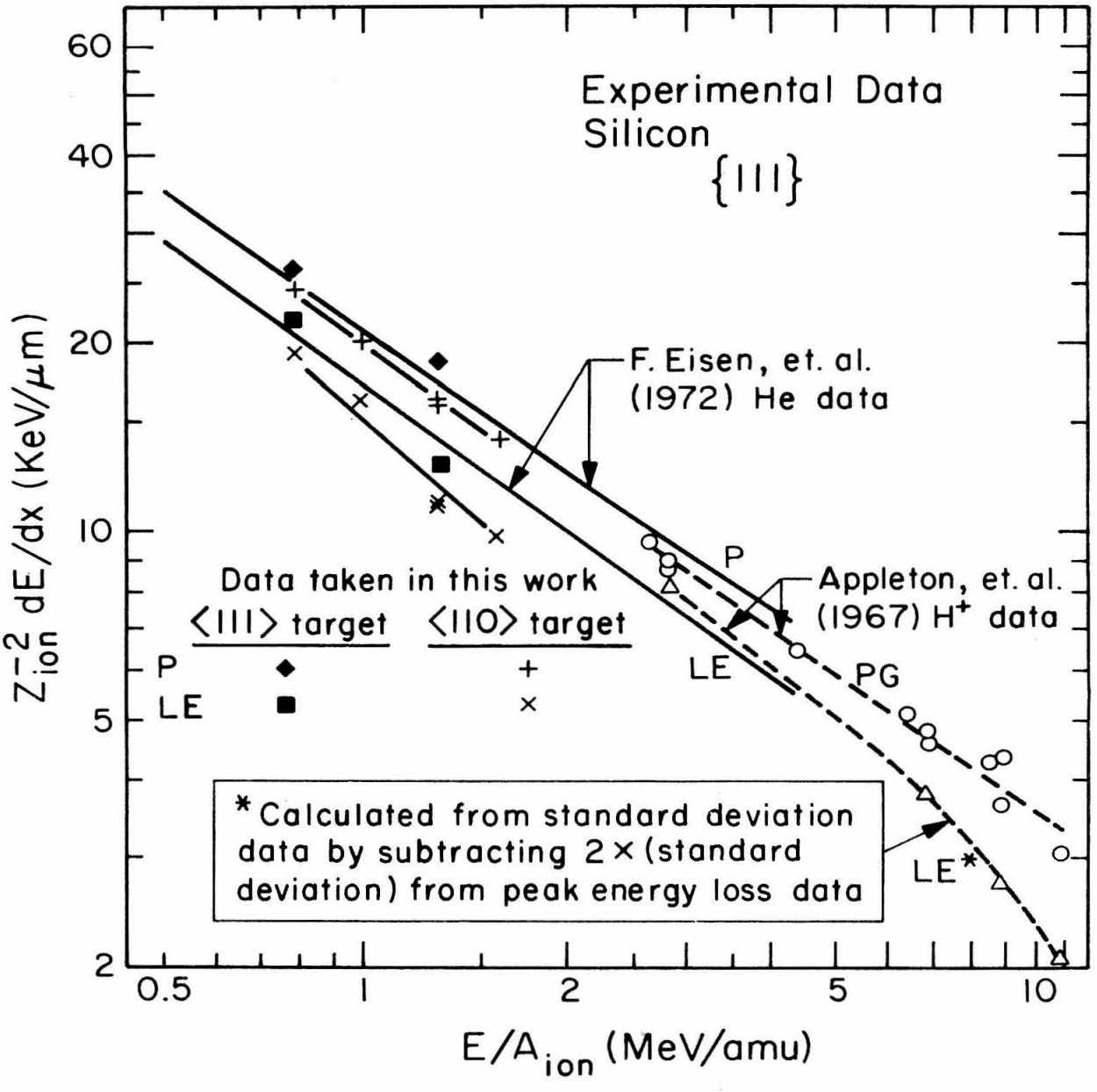
Experimental Data
Silicon
{111}
F. Eisen, et. al.
(1972) He data
Appleton, et. al.
(1967) H+ data
P
PG
LE
LE*
Data taken in this work
<111> target
<110> target
P
LE
*Calculated from standard deviation data by subtracting 2 × (standard deviation) from peak energy loss data
60
40
20
10
5
2
0.5
1
2
5
10
Z_{ion}^{-2} dE/dx (KeV/μm)
E/A_{ion} (MeV/amu)

Figure 11(f)

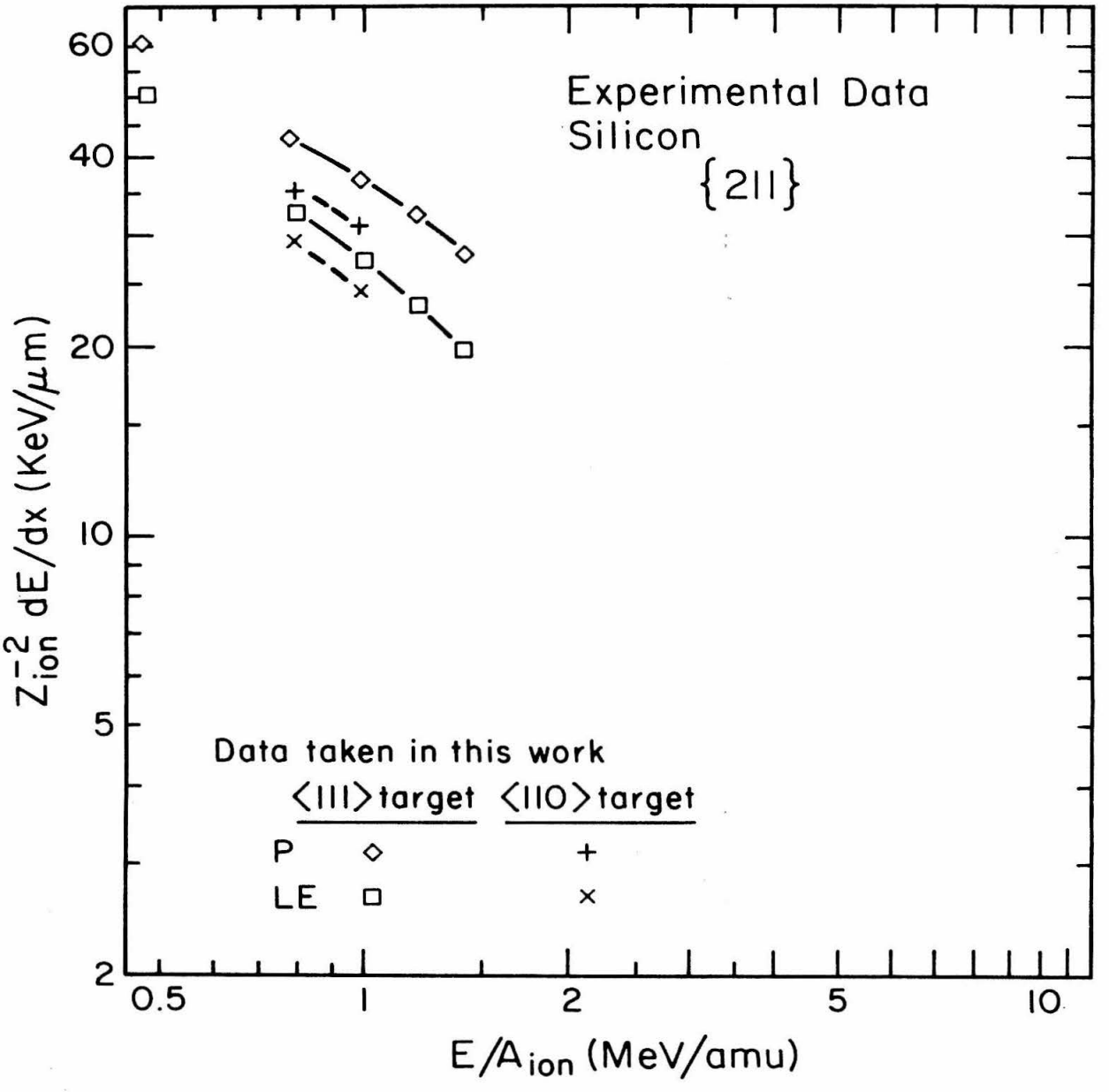
Experimental Data
Silicon
{211}
Data taken in this work
<111> target
<110> target
P
LE
60
40
20
10
5
2
0.5
1
2
5
10
Z_{ion}^{-2} dE/dx (KeV/μm)
E/A_{ion} (MeV/amu)

Figure 11(g)

Figure 12

Example of a transmission spectrum taken by the magnet sweep system. The calculations of dE/dx are shown on the plot.

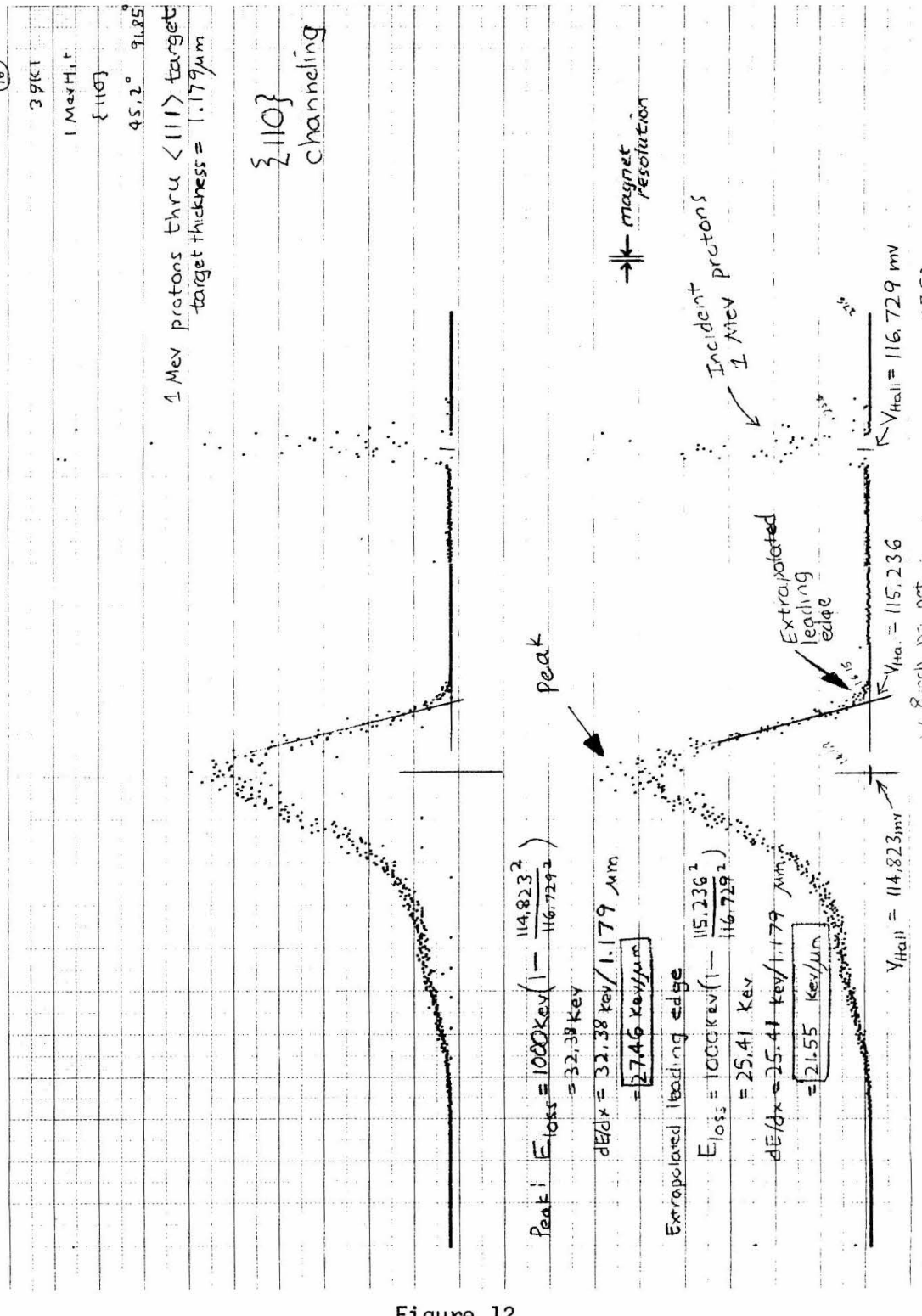
16
3 gkt
1 MeV H+
{110}
45.2°
91.85°
1 Mev protons thru <111> target
target thickness = 1.179 μm
{110}
channeling
magnet resolution
Incident 1 Mev protons
peak
Extrapolated leading edge
Peak! E_loss = 1000 Kev (1 − 114,823² / 116,729²)
= 32.38 Kev
dE/dx = 32.38 Kev / 1.179 μm
= 27.46 Kev/μm
Extrapolated leading edge
E_loss = 1000 Kev (1 − 115,236² / 116,729²)
= 25.41 Kev
dE/dx = 25.41 Kev / 1.179 μm
= 21.55 Kev/μm
V_Hall = 114,823 mv
V_Hall = 115,236
V_Hall = 116,729 mv
112.00 mv
117.53 mv

Figure 12

separate symbol for each datum) since a large number of different channels were investigated on this run. Solid symbols are used on the plot to distinguish the data from those of the earlier run.

These data showed consistently higher energy loss than the previous data, probably due to the carbon deposit and perhaps crystal damage from the target's long use. We will therefore not concern ourselves with these disagreements.

Two accelerator runs were carried out with the <110> target. It was found that locating the optimal channeling orientation was quite difficult. The <110> axis, being very broad, presented little problem. But the various planar channels intersecting at the <110> axis give very different energy loss values for slight changes in orientation. As was mentioned before in subsection VF, optimizing the visual pattern on the scintillator screen worked better than maximizing transmitted beam through the magnet, but not entirely satisfactorily. In the end spectra were taken at $.05^{o}$ intervals across the channels. This gave much more consistent results.

3. Comparison of the Data Taken in the Same Channels on the Two Targets

The {211} transmission spectra taken with the <111> target were rather broad and extended into the random spectrum region. This was not so for the {211} spectra obtained with the <110> target which showed nice channeling peaks. Therefore the <110> crystal data are probably more reliable. In the <111> , {110} , and {111} plots, we may disregard discrepancies with the second run <111> target data (solid symbols). For the {110} and random orientations, the two targets give compatible results.

4. Comparison with Data in the Literature

Available dE/dx data in the literature for light ions channeling in silicon have also been plotted in Figure 11. In all cases but those of Della Mea, et al. (1972) and F. Eisen, et al. (1972), data points and a fitted curve are given. In the case of these two researchers, only smooth curves drawn through their distributions of data points are shown in Figure 11 for simplicity, because the number of data points they present is quite large.

All data are converted to equivalent proton energy loss data. The form of equation (12) shows that this can be done by plotting $-Z_{ion}^{-2}\ dE/dx$ as a function of E/A_{ion}, where A_{ion} is the atomic mass of the incident ion in proton masses.

All the data curves on the plots are labeled according to how they were determined from the transmission spectra: P = peak, LE = extrapolated leading edge, and PG = peak of the Gaussian distribution fitted to the high energy side of the transmission spectrum. We see that the data are not compatible in the sense $-dE/dx_P > -dE/dx_{PG} > -dE/dx_{LE}$.

The only experimenters with data in the energy range of our data are Della Mea, et al. (1972) and F. Eisen, et al. (1972). Since we are using targets provided by Eisen and are reducing the data in terms of peak and extrapolated leading edge energy losses as he did, the most direct comparison can be made with his data.

In general, Eisen's data give lower energy losses than Della Mea's, and our data give still lower energy losses, with our lowest points compatible with Eisen's lowest points. The Eisen, et al. data

are for helium. Thus our contribution to the literature of data has been to obtain measurements for low energy protons compatible with these measurements in the <110>, <111>, and {111} channels, and then to obtain data in a larger number of different channels than has been previously examined.

F. Eisen, et al. and Della Mea, et al. obtained data that lie on lines parallel to each other (having the same energy loss dependence). This is not true for several of our curves. The peak energy loss curve for <111> channeling and the extrapolated leading edge energy loss curves for <111> and {111} channeling have steeper downward slopes than the F. Eisen and Della Mea curves. This may be due to straggling observed in our system peculiar to the system. Note that the lesser slope of the F. Eisen and Della Mea curves is in agreement with the theoretical calculations of dE/dx (see Figure 1).

B. Comparison of Experimental and Theoretical Values for dE/dx

By matching the plots in Figures 1 and 11, Z_{loc} values for the data of various experimenters were obtained. The results of this matching are given in Table 3.

Comparison of this table with Table 4 in Appendix A which gives values for Z_{loc} extracted from the averaged Thomas Fermi potential

by applying $\nabla^2 V = 4\pi\rho$ show the interesting result that for almost all of Della Mea's data and all of our data except {110} and {211}, the calculated Z_{loc} lies between the values of Z_{loc} that fit the peak (P) and the extrapolated leading edge (LE) of the spectra. If the actual Z_{loc} are those given in Table 4, and if only path variation straggling plays a role as F. Eisen, et al. claim, then one would expect $Z_{loc}^{table\ 4} = Z_{loc}^{(LE)}$. If only statistical straggling plays a role, one would expect $Z_{loc}^{table\ 4} = Z_{loc}^{(P)}$. Thus it looks as though both types of straggling contribute, if the theory is reliable.

To test the compatability of this conclusion with the theoretically expected straggling, we divide the difference of the energy loss obtained from Figure 1 using Z_{loc} from Table 4, and the LE energy loss from Figure 11, by the straggling value ΔE obtained from equation (27) using Z_{loc} from Table 4 and an average target thickness of 1.2 μm. The results are 1.4 to 2.1 for <110> , 1.5 to 1.9 for <111>, 1.4 for <211>, 2.1 for {100}, 2 to 2.5 for {111}, and 4.1 to 5.1 for {211}. These values are to be compared to 1.25 expected from the equation preceding (26), or 2 (see Section VII). We see that the data are not sufficiently accurate to give a conclusive test.

We conclude that the data taken give some support for the theory of energy loss summarized, and is order of magnitude compatible with the theory of straggling. Furthermore, new measurements of greater accuracy would be immediately useful for making a more accurate test.

Table 3

Results of the match of the experimental data with the calculations. The references are (1) this work, (2) Appleton, et al. (1967), (3) Eisen, et al. (1972), (4) Della Mea, et al. (1972), and (5) Clark, et al. (1970). P stands for peak, PG for peak of the Gaussian fitted to the high energy side of the spectrum, LE for extrapolated leading edge. In the fourth column, — indicates that the data are not in a region where an onset of core electron contributions occurs. Errors are obtained as described in VI C.

Table 3A

Channel	Reference		Z_{loc}	Onset of core energy losses accounted for?
<110>	1	P:	2.9± .5	-
		LE:	1.4 ± .4	-
	3	P:	3.2	-
		LE:	1.9-1.5	-
	4	PG:	4	-
	5	P:	5	Yes
		LE:	3.2	No
<111>	1	P:	5-4.5± .8	-
		LE:	4.3-3.3 ± .7	-
	3	P:	5	No
		LE:	3.8	No
	4	PG:	5-5.2	Yes, at 50% higher energy than calculated
	5	P:	4.5	-
		LE:	3.2	-
<211>	1	P:	4.5 ± .8	-
		LE:	3-2.3 ± .5	-
	4	PG:	4	Yes
	5	P:	5.2	No core contribution assumed
		LE:	3.7	

Table 3B

Channel	Reference	Z_{loc}	Onset of core energy losses accounted for?
{100}	1	P: 5-4.7±.9	-
		LE: 3.7-2.8±.7	-
{110}	1	P: 5 ± .8	No
		LE: 4.3-2.7 ± .6	No
	2	PG: 4.2	-
{111}	1	P: 3.1 ± .6	-
		LE: 2.2-1.7 ± .5	-
	2	PG: 2.7	
		LE: 2 , downward	No
	3	P: 3.5	No
		LE: 2.4	No
{211}	1	P: 4 ± 1	Perhaps
		LE: 2.8 ± .8	Perhaps

C. Analysis of Errors

1. Energy Calibration

In section VB we found that the error in the data due to incident beam energy and magnet sweep energy calibration to be 1%.

2. Target Thickness Variation

When the target was mounted under sodium light, it was observed that the thinnest region, positioned over the .015" diameter hole of the holder, fell between fringes. Thus, the thickness variation was under a quarter wavelength, around $1000\text{Å}/1\mu m = 10\%$ peak to peak. This gives a standard deviation of 3%.

Both the energy loss measurements and the Cary 14 target thickness measurements average the thickness variation to order $.03^2 \simeq .1\%$ (negligable). Therefore the peak of the transmission spectra will hardly be shifted by this variation. The shape of the spectra will be broadened by the effect of convolution with a distribution of width equal to 3% of the energy loss. For the data in Figure 12, this width is around 1 KeV. The peak minus the extrapolated leading edge energy loss is around 7 KeV. For a Gaussian distribution, this implies that the standard deviation is 3.5 KeV. Thus, target thickness variation introduces an error of $[(3.5^2 + 1^2)^{1/2} - 3.5]/3.5 = 4\%$. The other spectra give a similar number for the effect of target thickness variation.

3. Target Alignment

The data taken after the most careful alignments of the target

gave the lowest dE/dx values and in many cases fell on a smooth curve to an accuracy of better than 3%. Lines in Figure 11 show these smooth curves.

For a given target the scatter in the data is probably due to alignment difficulty. In the <111> data, averages of which are given by open symbols in Figure 11, the scatter was generally 1 to 3%. For the <110> data, the standard deviation of the scatter can be observed in Figure 11 to be around 4%. These errors give a probable upper limit to the error in the minimum dE/dx measurements due to target alignment.

4. Beam Width

Again referring to Figure 12, which is a representative sample of the data taken, the standard deviation of the beam width is about 1 KeV. As is argued in 2 above, this causes a broadening of the spectrum of around 4%. To correct for this error, the leading edge energy loss values from our data have been increased by 4% before the value of Z_{loc} given in Table 3 was obtained.

5. Beam Divergence

The beam divergence was found to be $.011^{o}$. (See section V G.) Ψ_{max} for 1 MeVprotons in the{111} channel in silicon is around $.4^{o}$. Thus, we see from the discussion of path variation straggling (III B) that the effect of beam divergence is much smaller than the effect of particles entering the channel with various impact parameters with respect to the channel center. We will neglect beam divergence.

6. Extraction of Data from the Plots of the Transmission Spectra

As was stated in subsection VI A, repeated measurements on the same target often gave results consistent with each other to 1%. We will take 1% as the error introduced when locating the relative peak and extrapolated leading edge and incident beam peak locations on a transmission spectrum.

All of the above errors (except 4, which is subtracted out) combine to give us an error bar of $(1^2 + 4^2 + 4^2 + 1^2)^{1/2} = 6\%$. This error is compared with the curves in Figure 1 to obtain the errors given in Table 3 for the Z_{loc} values extracted from our data.

VII. MOLECULAR CHANNELING

When an H_2^+ molecule enters a crystal, it loses its electron according to current theories. Then one would expect the two protons to push apart, and if they channel, to channel at a sufficient distance from each other that they would have the standard single proton energy loss. The idea was explored that if the two protons happen to enter the crystal one behind the other, the first might deflect enough nearby electrons to create a path for the second. If the second proton had a lower rate of energy loss as a result, it would nudge the first from behind. They would channel all the way through the crystal one behind the other with a net reduced energy loss. The configuration would be stable by energy arguments since if they separate, their energy loss would become greater.

Various models were tried to estimate the reduction in energy loss that might be expected for 1 MeV protons. All the models which allowed the phenomenon to occur gave an estimate of 2 to 9 KeV.

It was decided to try to examine the problem of whether or not this reduced molecular energy loss occurred experimentally.

First, gross effects were looked for. Transmission spectra for .8 Mev and 1.0 MeV protons were compared with 1.6 and 2.0 MeV H_2^+ data. The H_2^+ data did have a reduced energy loss. But when correction was made for the spreading of the incident beam energy spectrum that occurs after the H_2^+ enter the crystal target because of the H_2^+ dissociation energy, the effect disappeared to the order of the scatter in

the data points. The method of correcting the H_2^+ spectrum was (1) to obtain a standard deviation from

$$E_{out,LE} - E_{out,P} = 2\sigma$$

a relationship which holds exactly for a Gaussian distribution, (2) to obtain σ' by

$$\sigma'^2 = \sigma^2 - \sigma^2_{H_2^+ \text{ decomposition}}$$

and then (3) to compute

$$E_{out,P} + 2\sigma'$$

for the energy to be compared with the leading edge of the proton spectrum.

Second, an attempt was made to find a very small reduced energy loss peak above the leading edge of an H_2^+ transmission spectrum. The H_2^+ transmission spectrum was taken with the magnet sweep system and with a typical current through the final 8 inch magnet slit of 10^7 to 10^8 particles/sec. This beam, being much too large to be counted by a solid state detector without damaging the detector, was allowed to hit a copper tube. The scattered protons were counted by an off-axis detector. After the sweep system had scanned across the transmission spectrum to its leading edge, the detector was shifted into the beam line. As the sweep continued a Gaussian-like tail was observed (part of the high energy end of the transmission spectrum) but no fine detail indicating any molecular channeling effect.

APPENDICES

A. GEOMETRICAL INFORMATION ABOUT CHANNELS IN SILICON

Figures 13 and 14 give geometrical descriptions of low index axial and planar channels in silicon. Data for other diamond crystal structure substances can also be extracted from these figures by scaling all distances by the other substance's lattice constant, linear densities by its reciprocal, and planar densities by its reciprocal squared.

Figure 15 gives the graph of the plane averaged Thomas Fermi potential for the {110} channel.

Table 4 gives quartic fits to the row and plane averaged Thomas Fermi potentials computed for various channels, and also values of $Z_{loc}^{(0)}$ and $Z_{loc}^{(2)}$ obtained from the quartic fit potential by applying Maxwell's equation

$$\nabla^2 V = 4\pi\rho$$

Figure 13

Geometries of axial channels <1,0,0> , <1,1,0> , <1,1,1> , and <2,1,1> in silicon

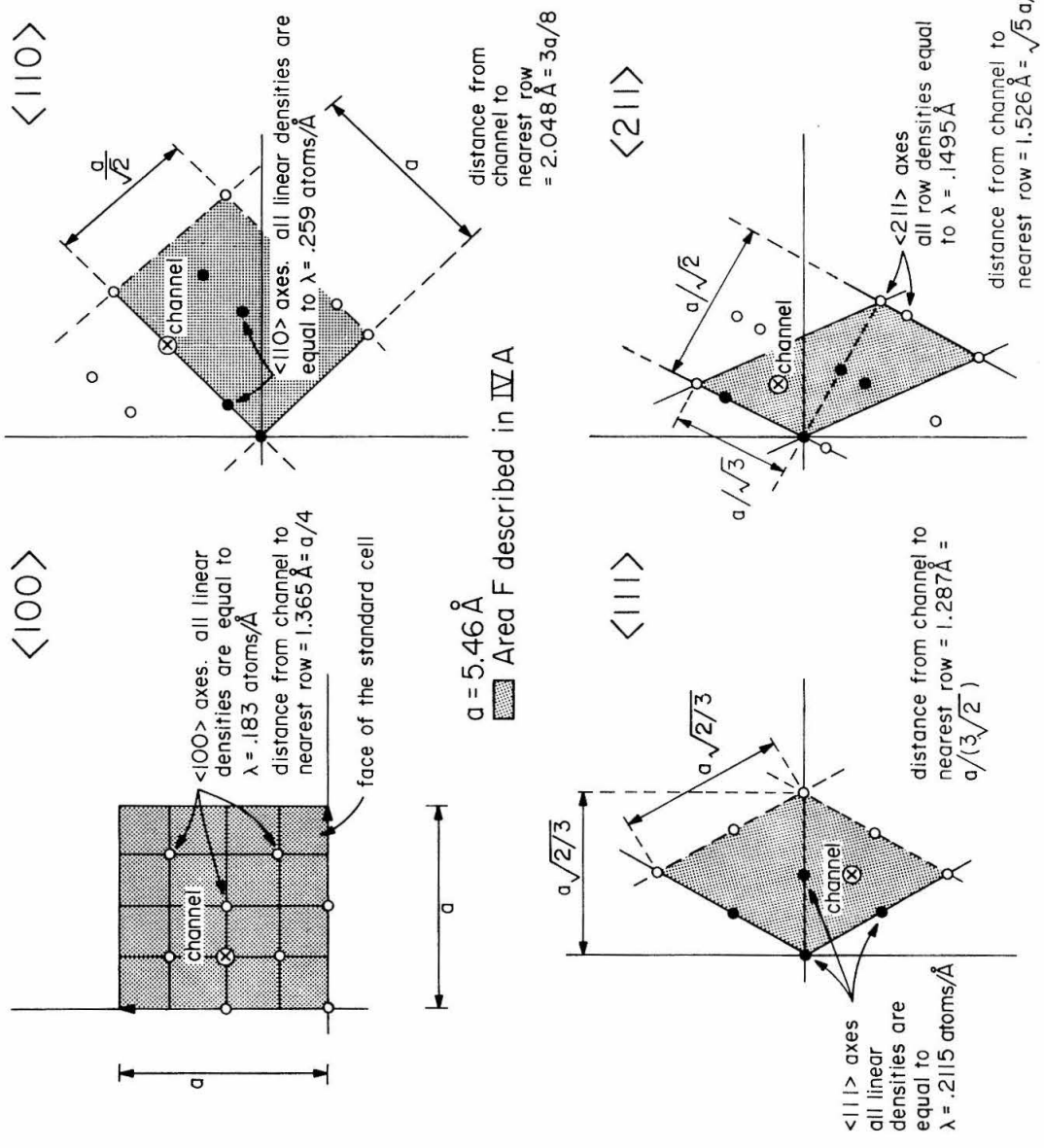
<110>
a/√2
channel
<110> axes. all linear densities are equal to λ = .259 atoms/Å
a
distance from channel to nearest row = 2.048 Å = 3a/8
<100>
<100> axes. all linear densities are equal to λ = .183 atoms/Å
distance from channel to nearest row = 1.365 Å = a/4
face of the standard cell
channel
a
a
a = 5.46 Å
Area F described in IV A
<211>
a/√2
channel
a/√3
<211> axes all row densities equal to λ = .1495 Å
distance from channel to nearest row = 1.526 Å = √5 a/8
<111>
a√2/3
a√2/3
channel
distance from channel to nearest row = 1.287 Å = a/(3√2)
<111> axes all linear densities are equal to λ = .2115 atoms/Å

Figure 13

Figure 14

Geometries of planar channels {1,0,0} , {1,1,0} , {1,1,1} , and {2,1,1} in silicon

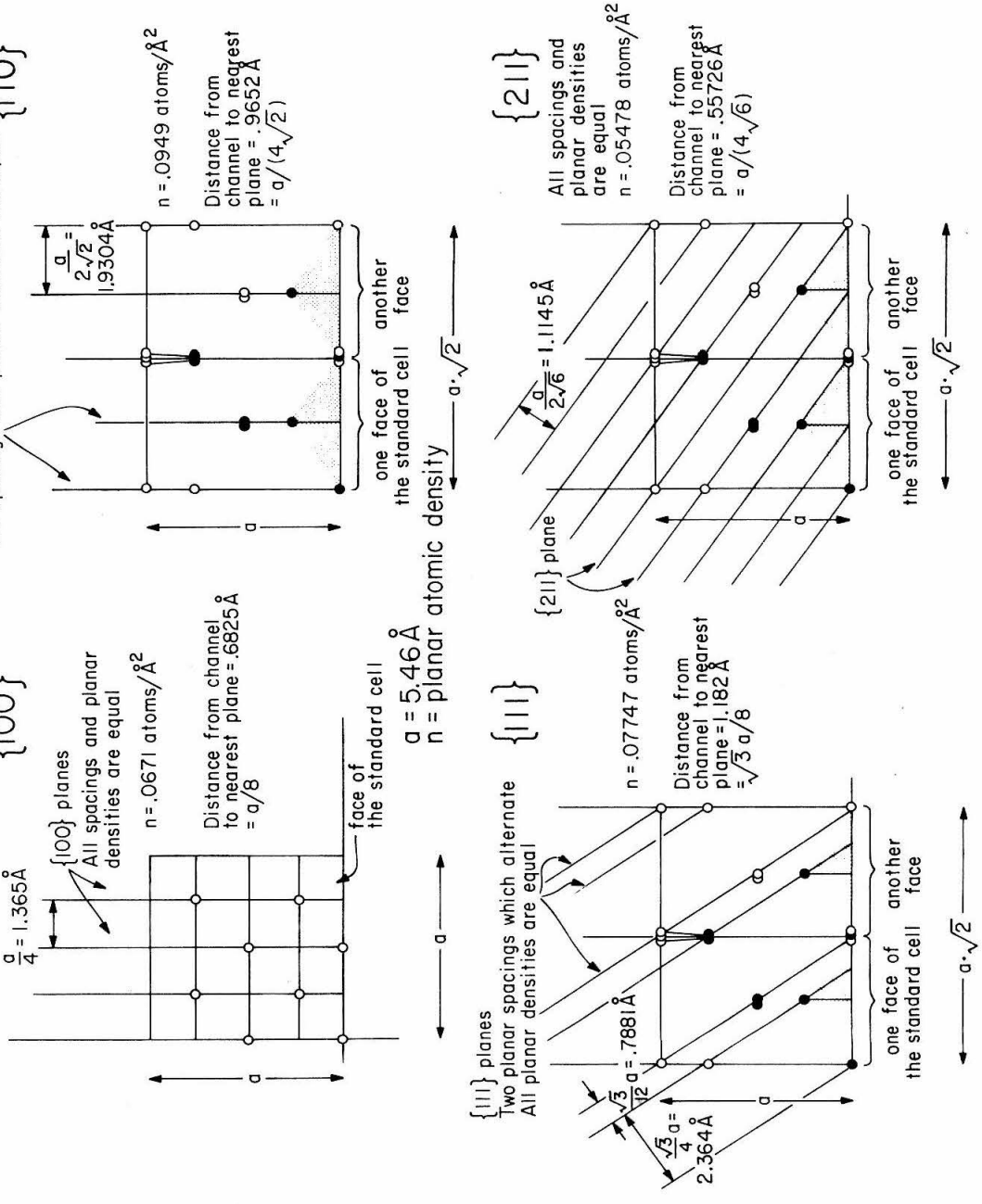
{100}
{100} planes
All spacings and planar densities are equal
a/4 = 1.365Å
n = .0671 atoms/Å²
Distance from channel to nearest plane = .6825Å = a/8
face of the standard cell
a
a = 5.46Å
n = planar atomic density
{110}
{110} planes
All spacings and planar densities are equal
a/2√2 = 1.9304Å
n = .0949 atoms/Å²
Distance from channel to nearest plane = .9652Å = a/(4√2)
one face of the standard cell another face
a·√2
{111}
{111} planes
Two planar spacings which alternate
All planar densities are equal
n = .07747 atoms/Å²
Distance from channel to nearest plane = 1.182Å = √3 a/8
√3/12 a = .7881Å
√3/4 a = 2.364Å
one face of the standard cell another face
a·√2
{211}
{211} plane
All spacings and planar densities are equal
n = .05478 atoms/Å²
Distance from channel to nearest plane = .55726Å = a/(4√6)
a/2√6 = 1.1145Å
one face of the standard cell another face
a·√2

Figure 14

Figure 15

Graph of the Plane Averaged Thomas Fermi potential for the {110} axis of silicon. A quadratic fit is indicated.

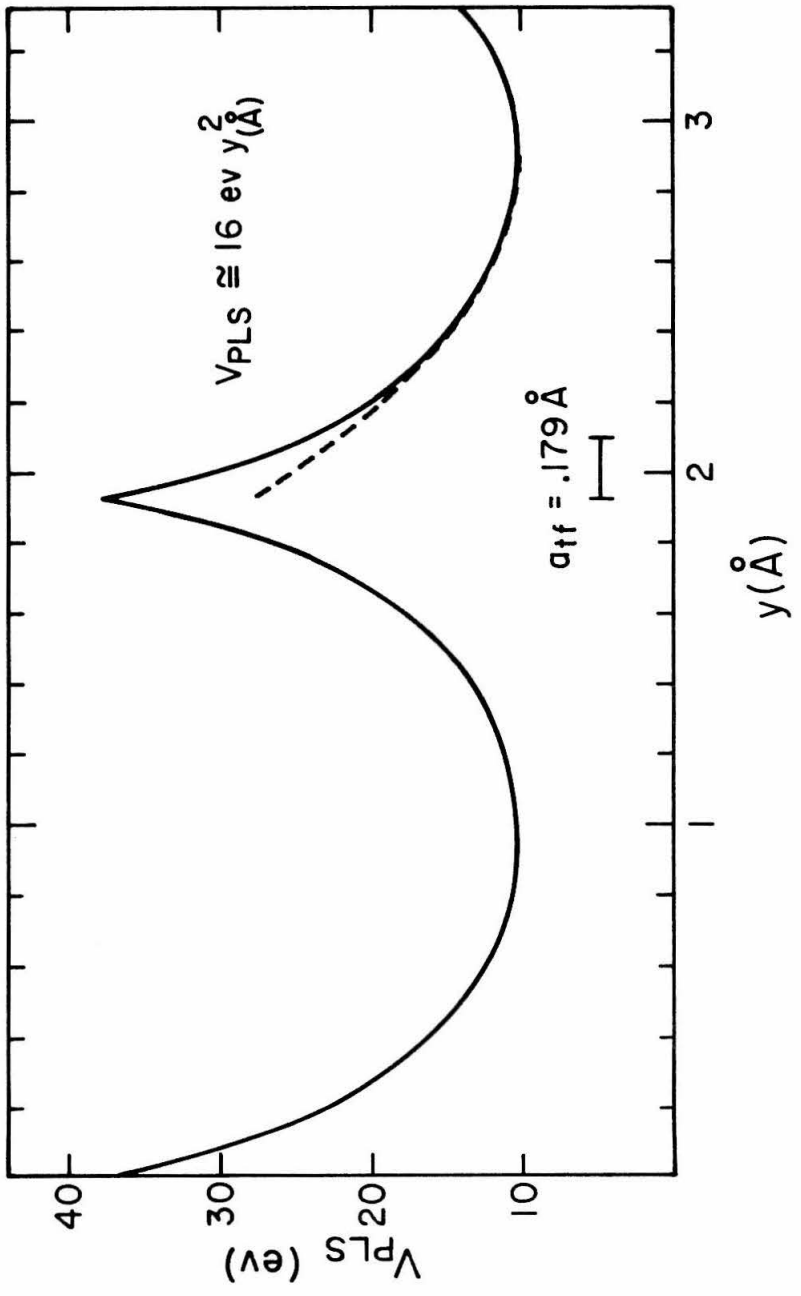

Figure 15

Table 4

Coefficients of the quartic fit to row and plane averaged Thomas Fermi potentials and corresponding values of $Z_{loc}^{(0)}$ and $Z_{loc}^{(2)}$. For axial channels, the row averaged potential is averaged over angles about the channel center by a ten point numerical integration before the quartic fit is made. A and B in the table are defined in terms of the plane or angular averaged row potential V by

$$V(x) \cong Ax^2 + Bx^4 + \text{constant}$$

where x is the distance from the channel center in $\mathring{A}$. The fit is made by requiring this equation to be exact for $x = 0$, $x = \frac{1}{3} x_m$, and $x = \frac{2}{3} x_m$ where x_m is the distance from the channel center to the nearest row or plane. $Z_{loc}^{(0)}$ and $Z_{loc}^{(2)}$ are computed from

$$\nabla^2(Ax^2 + Bx^4) = 4\pi eN(Z_{loc}^{(0)} + Z_{loc}^{(2)} x^2)$$

This reduces to $Z_{loc}^{(0)} = c_0 A/(4\pi eN)$ and $Z_{loc}^{(2)} = c_2 B/(4\pi eN)$ where (1) in the axial case where x is a cylindrical radial variable, $c_0 = 6$ and $c_2 = 20$, and (2) in the planar case, $c_0 = 2$ and $c_2 = 12$.

Table 4

Channel	Coefficients of the quartic fit		Local number of electrons per atom	
	$A(\frac{eV}{\mathring{A}^2})$	$B(\frac{eV}{\mathring{A}^4})$	$Z_{loc}^{(0)}$	$Z_{loc}^{(2)}(\frac{1}{\mathring{A}^2})$
<100>	6.34	1.98	4.29	4.46
<110>	3.35	.77	2.26	1.73
<111>	6.67	2.28	4.50	5.12
<211>	4.65	1.24	3.14	2.79
{100}	20.72	21.95	4.66	29.63
{110}	15.02	9.02	3.38	12.17
{111}	10.13	4.03	2.28	5.44
{211}	24.90	34.04	5.60	45.94

B. DESCRIPTION AND STABILITY ANALYSIS OF THE MAGNET HALL PROBES AND CONTROL CIRCUITS

Besides magnetic field, there are two controllable variables that affect the Hall probe voltage, temperature and control current.

The Hall probe voltage is directly proportional to the control current. All three Hall probes used are connected to highly regulated current power supplies. In the control circuit for the old Hall probe, the control current passes through a 1Ω wire wound resister. The voltage across that resister, V_{cc}, is measured by a 4-1/2 digit Weston panel digital voltmeter and is adjusted manually to 100.00 mv each time the Hall probe voltage is read. In each of the two new Hall probes' control circuits illustrated in Figure 16(a), the control current is passed through an 8Ω Kelvin Electric Company 5 ppm/^{o}C shunt resistor. The voltage V_{cc} dropped across this shunt is compared with and made to equal the output of an 8 ppm/^{o}C one-volt reference circuit by means of a Precision Monolithics model OP-05C operational amplifier. This amplifier is a chopperless IC device with typical voltage offset drift ratings of 3μv/^{o}C and 2.5 μv/month. (A chopper stabilized operational amplifier with better specifications is recommended to anyone who duplicates the circuit.)

The mean temperature coefficients of the Siemen's FC34 Hall probes used are specified to be -.04%/^{o}C for the open circuit voltage and +.2%/^{o}C for the internal resistance. The 50Ω terminating the Hall

Figure 16

Control current and temperature regulation circuit for each of the new Hall probes

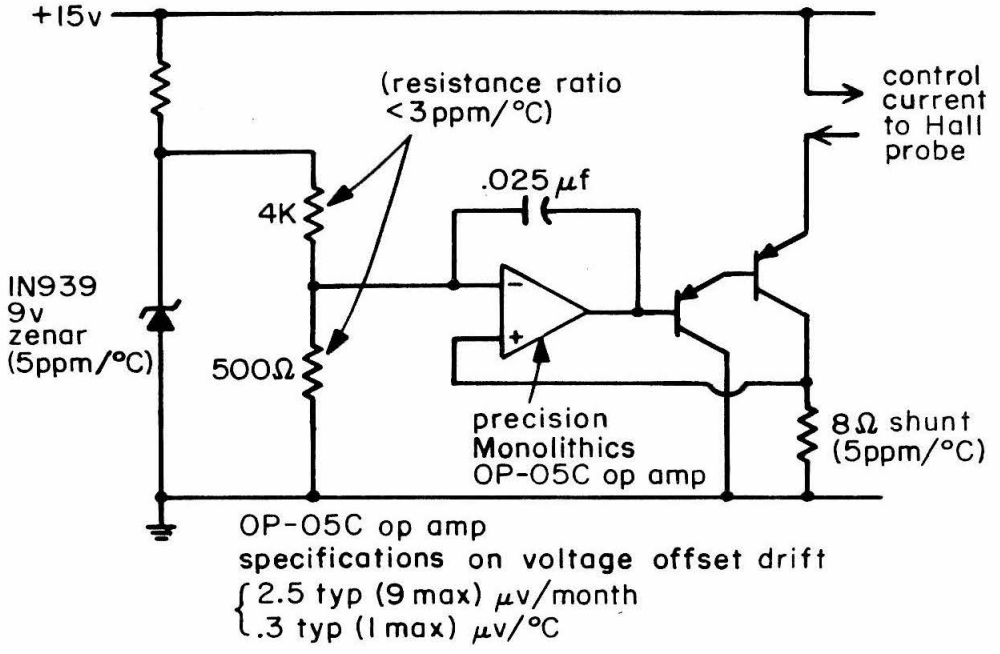

(a) control current regulating circuit

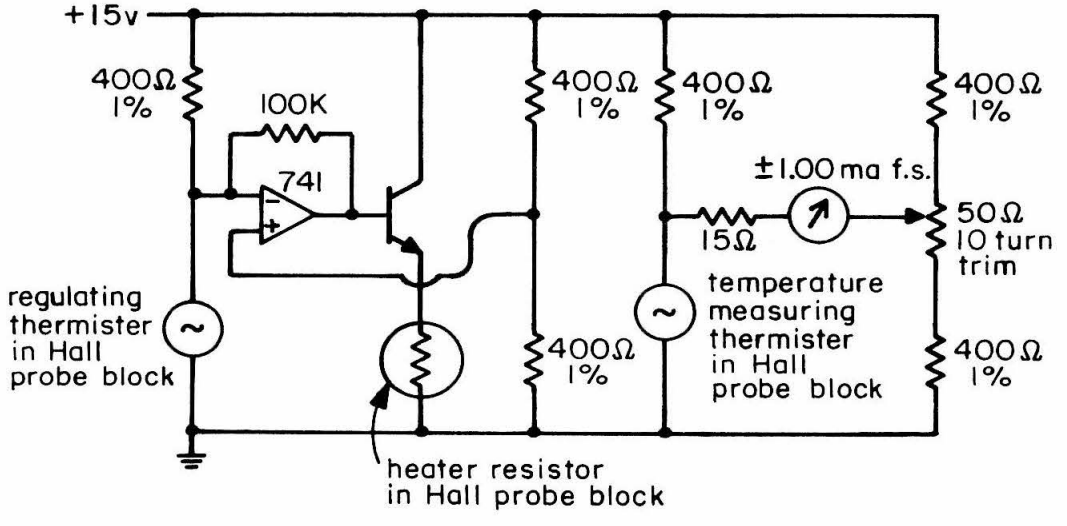

(b) temperature regulating circuit

Figure 16

voltage output is 10 to 15 times the internal resistance. Therefore, both coefficients combine to give a mean temperature coefficient of approximately -.06%/^{o}C for the observed Hall probe voltage.

The Hall probes are mounted in copper blocks which contain a heating resistor and two Fenwall Electronics Inc. model GB31P2 thermisters. One thermister controls the heating resister so as to maintain a constant temperature in the copper block. The other thermister is used to obtain an independent readout of the copper block temperature T for checking purposes. The temperature regulation circuit used with the new Hall probes is given in Figure 16(b).

The power supply that powers the new Hall probe control circuits puts out 15 volts nominally. When its voltage, which we call V_{PS} varies by 1% the control current shunt voltage was found to vary by .04% and the voltage across the temperature sensing thermister by 3.2% (which corresponds to a temperature change of -2.1 ^{o}C for the 90^{o} magnet and -3.7 ^{o}C for the 8 inch magnet).

Over a period of three months total variations of the following size were observed (average results for the two magnets)

Variable	Maximum Fluctuation	Resulting Fluctuation in V_{Hall}
V_{cc}	± .01%	± .01%
T	± .7 ^{o}C	± .04%
V_{PS}	± .2%	± .04%

The geometric mean of these V_{Hall} fluctuations is .06%.

REFERENCES

Appleton, B. R., Erginsoy, C., and Gibson, W. M. 1967, Phys. Rev. 161, 330.

Briggs, H. B. 1950, Phys. Rev. 77, 287.

Clark, G. J., Morgan, D. V., and Poate, J. M. 1970, in Atomic Collision Phenomena in Solids, edited by D. W. Palmer, M. W. Thompson, and P. D. Townsend (North Holland, Amsterdam), p. 389.

Della Mea, G., Drigo, A. V., Lo Russo, S., Mazzoldi, P., and Bentini, G. G. 1972, Rad. Eff. 13, 115.

Eisen, F. H., Clark, G. J., Bøttiger, J., and Poate, J. M. 1972, Rad. Eff. 13, 93.

Eisen, F. H. 1974, personal communication.

Fano, U. 1963, Ann. Rev. Nucl. Sci. 13, 1.

Hermann, F. and Skillman, S. 1963, Atomic Structure Calculations (Prentice Hall, Inc., Englewood Cliffs, N.J.).

Lindhard, J. 1954, Mat. Fys. Medd. Dan. Vid. Selsk. 28, no. 8.

Lindhard, J. 1965, Mat. Fys. Medd. Dan. Vid. Selsk. 34, no. 14.

Luntz, M. and Bartram, R. H. 1968, Phys. Rev. 175, 468.

Pines, D. 1964, Elementary Excitations in Solids (W. A. Benjamin, Inc., New York).

Roll, P. G., and Steigert, F. E. 1960, Phys. Rev. 120, 470.

Snyder, C. W. 1948, Ph.D. Thesis, California Institute of Technology.